Precursors_cci+

ESA Climate Change Initiative (CCI)

D2.2 (E3UB)

Title	D2.2 End to End ECV Uncertainty Budget
Reference	Precursors_cci+_D2.2_E3UB_01_02
Issue	01
Revision	02
Status	Final
Date of issue	24/06/2024
Document type	Deliverable

This work has received funding from the European Space Agency under Contract No 4000138243 and is the result of the cooperation between the partners of the Precursors_cci+ consortium.

Generated by KNMI

	FUNCTION	NAME	DATE
LEAD AUTHOR(S)		Folkert Boersma Isabelle De Smedt Nicolas Theys Lieven Clarisse Thomas Danckaert Sora Seo Pieter Valks Maya George	24/06/2024
REVIEWED BY	Science Leaders	M. Van Roozendael Folkert Boersma	24/06/2024 24/06/2024
	ESA Project Officer	Simon Pinnock	../../….
DISTRIBUTED TO	ESA Precursors_cci+ Consortium		

DOCUMENT CHANGE RECORD

Issue	Revision	Date	Modified items	Observations
0	0	15/09/2023	Initial template	Creation of document
1	0	01/10/2023	First issue of the document (version 1.0), containing descriptions of the uncertainty budget of L2 algorithms for all products	
1	1	15/12/2023	Revision of the document (version 1.1), addressing the RIDs raised by ESA in October 2023.	ESA accepted RIDs with the exception of the issue below.
1	2	24/06/2024	Revision to include previously missing update on CO uncertainty characterization.	

Table of Contents

Executive Summary

This document provides the theoretical uncertainty assessment of the ECV Precursor level-2 retrieval algorithms for NO2, HCHO, SO2, CO, NH3 and glyoxal in the ESA CCI+ ECV Precursor project. The purpose is to characterize the uncertainties in the entire retrieval process, from the impact of instrumental noise and degradation to uncertainties associated with the required input datasets. This leads to estimates of uncertainty magnitudes and patterns in time and space, which informs users about the relative strength of the level-2 satellite retrievals. A distinction is made between random and systematic contributions to the overall (pixel-specific) uncertainties. The document explains how the uncertainties are estimated, what their magnitudes are, and how the uncertainties should be interpreted to better understand the fitness-for-purpose of the ESA CCI+ ECV Precursor data. In the next version of this document, due in cycle 2 of the project, these level-2 uncertainties are input, together with known systematic aspects of the retrievals, to estimate the uncertainties in the level-3 products,

1. Purpose and scope

1.1. Purpose

This document describes the uncertainties associated with the level-2 retrieval algorithms in the Precursors_cci+ project. It addresses uncertainty estimates for the tropospheric NO2, HCHO, CO, SO_2, NH_3 and glyoxal retrievals.

1.2. Scope

The scope of this version of the E3UB is to fully describe the uncertainty budget for each retrieval algorithm used to derive the ECV products from input satellite data. This includes the general uncertainty propagation approach, the most important algorithm sensitivities, uncertainty estimates on ancillary data, and how these drive the overall pixel based L2 uncertainty budget. Examples will be given on spatio-temporal patterns in L2 uncertainties.

The E3UB focuses on level-2 retrieval algorithm uncertainties on a per-pixel basis. At a later stage, in cycle 2 of the project, the E3UB will provide detailed information on level-3 uncertainties.

We focus here on the following questions relevant to users of ESA CCI+ ECM Precursor retrievals:

- What is the origin of the uncertainties in the final ECV Precursor product, and how do the uncertainties propagate in the retrieval procedure?
- Which uncertainty contributions are random, and which are systematic?
- What is the distribution of uncertainty patters in space and time?
- What does this mean for user applications of the ECV Precursor data?

1.3. Applicable documents

[AD-1] Data Standards Requirements for CCI Data Producers. Latest version at time of writing is v1.2: ref. CCI-PRGM-EOPS-TN-13-0009, 9 March 2015, available online at: https://climate.esa.int/media/documents/CCI_DataStandards_v2-3.pdf

[AD-2] CCI Data Policy v1.1. Available online at: https://climate.esa.int/sites/default/files/CCI_Data_Policy_v1.1.pdf

1.4. Reference documents

[RD-1] GCOS Climate Monitoring Principles, November 1999. Available online at: https://gcos.wmo.int/en/essential-climate-variables/about/gcos-monitoring-principles

[RD-2] Guideline for the Generation of Satellite-based Datasets and Products meeting GCOS Requirements, GCOS Secretariat, GCOS-128, March 2009 (WMO/TD No. 1488).

Available online at: https://library.wmo.int/index.php?lvl=notice_display&id=12884#.Yw4rL7RByUk

[RD-3] Quality assurance framework for earth observation (QA4EO): http://qa4eo.org

[RD-4] The Global Observing System for Climate: Implementation Needs, GCOS-200, October 2016. Available online at: https://gcos.wmo.int/en/gcos-implementation-plan

[RD-5] Status of the Global Observing System for Climate, GCOS-195, October 2015. Available online at: https://library.wmo.int/index.php?lvl=notice_display&id=18962#.Yw4r8LRByUk

[RD-6] Hollmann, R., et al., The ESA climate change initiative: Satellite data records for essential climate variables. American Meteorological Society. Bulletin, Vol. 94, No. 10, 2013, p. 1541-1552.

[RD-7] Joint Committee for Guides in Metrology, 2008, Evaluation of measurement data — Guide to the expression of uncertainty in measurement (GUM), JGCM 100: 2008. Available online at: https://www.iso.org/sites/JCGM/GUM-JCGM100.htm

[RD-8] Merchant, C., et al., 2017, Uncertainty information in climate data records from Earth observation, Earth Syst. Sci. Data Discuss., vol. 9, p511-527

1.5. List of acronyms

AC-SAF	Satellite Application Facility on Atmospheric Composition Monitoring
ADP	Algorithm Development Plan
AK	Averaging Kernel
AMF	Air-mass factor
ATBD	Algorithm Theoretical Basis Document
BIRA-IASB	Royal Belgian Institute for Space Aeronomy
BIRA-IR	BIRA-IASB Infrared Team
BIRA-SYN	BIRA-IASB Synergy Team
BIRA-UVVIS	BIRA-IASB UV-Vis Team
BIRA-MOD	BIRA-IASB Tropospheric Modeling Team
CAMS	Copernicus Atmospheric Monitoring Service
C3S	Copernicus Climate Change Monitoring Service
CCI	ESA Climate Change Initiative
CCI+	Climate Change Initiative Extension (CCI+), is an extension of the CCI over the period 2017-2024.
CEOS	Committee on Earth Observation Satellites
CMUG	Climate Modeling User Group
CO	Carbon monoxide
COBRA	COvariance-Based Retrieval Algorithm
CRDP	Climate Research Data Package

CRG	Climate Research Group
DLR	German Aerospace Centre
DOAS	Differential Optical Absorption Spectroscopy
ECMWF	European Centre for Medium-range Weather Forecast
ECV	Essential Climate Variable
ENVISAT	Environmental Satellite (ESA)
EO	Earth Observation
ESA	European Space Agency
EU	European Union
EUMETSAT	European Organisation for the Exploitation of Meteorological Satellites
FCDR	Fundamental Climate Data Record
FRESCO	Fast Retrieval Scheme for Clouds from the Oxygen A band
FRM	Fiducial Reference Measurement
GCOS	Global Climate Observation System
GOME	Global Ozone Monitoring Instrument (aboard ERS-2)
GOME-2	Global Ozone Monitoring Instrument – 2 (aboard MetOp-A, -B and -C)
IASI	Infrared Atmospheric Sounding Interferometer
HRI	Hyperspectral Range Index
KNMI	Royal Netherlands Meteorological Institute
LEO	Low Earth Orbit
LUT	Look-up table
Metop	Meteorological Operational Platform (EUMETSAT)
MOPITT	Measurement of Pollution in the Troposphere
NASA	National Aeronautics and Space Administration
NDACC	Network for the Detection of Atmospheric Composition Change
NH_3	Ammonia
NN	Neural Network
NO_2	Nitrogen dioxide
NRT	Near-Real Time
OCRA	Optical Cloud Recognition Algorithm)
OMI	Ozone Monitoring Instrument (aboard EOS-Aura)
PCA	Principal Component Analysis
QA4ECV	Quality Assurance for Essential Climate Variables
QA4EO	Quality Assurance framework four Earth Observation
R&D	Research and Development
ROCINN	Retrieval of Cloud Information using Neural Networks
SAF	Satellite Application Facility
SCIAMACHY	Scanning Imaging Absorption Spectrometer for Atmospheric
S5P	Sentinel-5 Precursor
SoW	Statement of Work
STREAM	STRatospheric Estimation Algorithm from Mainz
SZA	Solar Zenith Angle
TEMIS	Tropospheric Emission Monitoring Internet Service
TIR	Thermal Infrared spectral range
TROPOMI	Tropospheric Monitoring Instrument (aboard Sentinel-5 Precursor)

TOA	Top-of-atmosphere
TOAR-II	Tropospheric Ozone Assessment Report Phase-II
ULB	Université Libre de Bruxelles
IUP-UB	Institute of Environmental Physics, University of Bremen
UPAS	Universal Processor for UV/Vis Atmospheric Sensors
UV-Vis	Ultraviolet and visible spectral range
WP	Work Package

2. Terminology

The uncertainty characterization in the ECV Precursors CCI follows, in general, the approach and recommendations from Merchant et al. (2017), applied widely in the CCI programme, and used previously in the QA4ECV project. The terminology follows international standards from metrology. We note the following definition of terms:

- *the measurand*: the quantity to be measured (here often the tropospheric vertical column density);
- *measurement*: the process of experimentally obtaining measured values that can be attributed to a quantity. In this project the *retrieval process*, or *retrieval* is sometimes understood to be the measurement;
- the *measured value*: the result of a measurement or a retrieval obtained to quantify the measurand;
- the *error*: the measured value minus the true value of the measurand. In practice the error is unknowable, except when the measured or retrieved value can be compared with a reference value of negligible uncertainty;
- the *uncertainty*: a non-negative parameter characterizing the dispersion (spread) of the quantity value attributed to the emasurand, given the measured value and an understanding of the measurement. The uncertainty estimates are central in this document.

For some of the trace gas level-2 algorithms discussed here, the terms *trueness* and *precision* are used.

- *trueness* is understood to represent an estimate of the systematic component to the uncertainty;
- *precision* is understood to represent the random contribution to the uncertainty estimate. The precision is often thought to cancel when averaging over multiple measured values.

3. Level-2 algorithms

3.1. Uncertainty assessment for tropospheric nitrogen dioxide (L2-NO2)

3.1.1. Uncertainty propagation

The retrieval procedure for tropospheric NO_2 consists of three distinct steps, and each contributes to the overall uncertainty. We therefore evaluate and propagate the uncertainties associated with each step: (1) the uncertainty in the total slant column originating from the spectral fitting, (2) the uncertainty in the background (stratospheric) correction,a nd (3) the uncertainty in the tropospheric air mass factor estimates, and (4) the overall algorithm uncertainty assessment resulting from the uncertainty propagation implemented for each individual pixel following the principles laid out in Boersma et al. [2004] and Boersma et al. [2018]. Specifically, the tropospheric NO_2 vertical column density is retrieved with the following equation:

$$N_{v,trop} = \frac{N_s - N_{s,strat}}{M_{trop}} \tag{3.1-1}$$

The main intermediate quantities of the retrieval algorithm are the slant column density (N_s), the tropospgeric air mass factor (M_{trop}), and the estimates for the stratospheric correction ($N_{s,strat}$). Through propagation of the uncertainties in all three intermediate quantities, we arrive at an uncertainty estimate for the tropospheric column at the algorithm level via Equation (3.1-2):

$$\sigma^2_{N_{v,trop}} = \left(\frac{\sigma_{N_s}}{M_{tr}}\right)^2 + \left(\frac{\sigma_{N_{s,strat}}}{M_{tr}}\right)^2 + \left(\frac{(N_s - N_{s,strat})\sigma_{M_{tr}}}{M^2_{tr}}\right)^2 \tag{3.1-2}$$

In Eq. (3.1.2), the (squared) air mass factor uncertainty is written as:

$$\sigma^2_{M_{tr}} = \left(\frac{\partial M_{tr}}{\partial A_s}\sigma_{A_s}\right)^2 + \left(\frac{\partial M_{tr}}{\partial f_{cl}}\sigma_{f_{cl}}\right)^2 + \left(\frac{\partial M_{tr}}{\partial p_{cl}}\sigma_{p_{cl}}\right)^2 + (\alpha M_{tr})^2 \tag{3.1-3}$$

where $\frac{\partial M_{tr}}{\partial A_s}$ represents the local sensitivity of the air mass factor to the surface albedo, σ_{A_s} the estimate of the uncertainty in the surface albedo, and so on. The last term on the right-hand side of Eq. (3.1.3) represents the contribution from uncertainty in the a priori NO_2 profile shapes and is estimated as ±10% (i.e. α=0.1) of the tropospheric air mass factor based on studies that replace a priori profile shapes with observed NO2 profiles or with simulated profiles from higher-resolution models in strongly polluted regions. Outside of those areas, in regions with no or modest pollution, the Round Robin pointed out that AMF uncertainty resulting from a priori profile shapes may be as high as 30% (i.e. α=0.3).

The contribution from uncertainties in the a priori profile is eliminated when NO_2 data users apply the averaging kernel (e.g. Rodgers (2000); Eskes and Boersma (2003); Boersma et al. (2016). The last term on the right-hand side in Eq. (3.1-3) may then be omitted. Using

averaging kernels, or recalculation of tropospheric air mass factors with the model simulations of interest (e.g. Visser et al. (2019)), allows for a better satellite-to-model comparison, by ensuring that the model is sampled consistent with the satellite retrievals, because identical assumptions are made on vertical sensitivity, and differences between the model's vertical NO2 distribution and the satellite a priori vertical NO_2 distribution then cancel.

3.1.2. NO_2 slant column density uncertainty estimates

Within the S5P and QA4ECV-projects, and in the Round Robin of this ECV Precursor project, much work has been done to characterize the magnitude and spatial patterns in NO2 slant column uncertainties from various sensors, especially for GOME-2A, OMI, and TROPOMI, and to better understand the sources of error that drive the uncertainty in the NO_2 slant columns. We summarize here the state-of-science in our understanding of the uncertainties in the NO_2 slant column densities (σ_{N_S}) for all sensors in this project.

Table 3.1.1 NO_2 slant column (statistical) uncertainties (typical, per pixel), and their trends, recently estimated in the QA4ECV, S5P, and ECV Precursor projects.

	Processor	**σ_{N_S} (random)**	**Trend**	**Reference**
GOME	QA4ECV (405-465 nm)	0.40×10^{15} molec. cm^{-2}		Boersma et al. (2004)
SCIAMACHY	QA4ECV (405-465 nm)	0.50×10^{15} molec. cm^{-2}		Boersma et al. (2008)
GOME-2A	QA4ECV AC-SAF[a]	0.73×10^{15} molec. cm^{-2} 0.47×10^{15} molec. cm^{-2}	3% yr^{-1} 5.2%yr^{-1}/1.8% yr^{-1} [b]	Zara et al. (2018) Seo et al. (2023)
GOME-2B	AC-SAF[a]	0.48×10^{15} molec. cm^{-2}	1.2% yr^{-1}	Seo et al. (2023)
GOME-2C	AC-SAF[a]	0.60×10^{15} molec. cm^{-2}	4.5 % yr^{-1}	Seo et al. (2023)
OMI	QA4ECV Coll4	0.76×10^{15} molec. cm^{-2}	1 % yr^{-1}	Zara et al. (2018); Anglou et al. (2023)
TROPOMI	Coll3	0.6×10^{15} molec. cm^{-2}	1.5 % yr^{-1}	van Geffen et al. (2020; 2022)

One lesson from earlier work is that the uncertainty in NO_2 slant column densities is spatially coherent and is mostly driven by random sources of error such as instrument noise. Uncertainty levels indeed depend on the reflectance level, with the darkest scenes having somewhat higher NO_2 uncertainties, and brighter scenes somewhat lower. The largest uncertainties typically occur close to areas with very high reflectance resulting from very bright (convective) clouds. On average, all-sky scenes (including cloudy areas) have some 10%

[a] The AC-SAF uncertainty estimates are reported here for 'all-sky' conditions, all other are for 'clear-sky' conditions, which are known to be substantially higher because of lower reflectances (Zara et al., 2018).
[b] Trends in GOME-2A NO2 slant column uncertainties before and after the second throughput test (September 2009). The first period is from January 2007 to September 2009, and the second is from October 2009 to December 2019.

lower NO2 uncertainties than clear-sky scenes (Zara et al., 2018), but we focus on the latter here, since these are the scenes relevant for tropospheric NO_2 retrievals.

To assess the NO_2 slant column uncertainties from three GOME-2 sensors on MetOp-A/B/C throughout their mission periods, we used a posteriori statistical approach that quantifies the spatial variability of the slant columns over clean Pacific regions used in previous studies (Boersma et al., 2007; Zara et al., 2018). This statistical method is useful to quantify the NO_2 slant column uncertainties derived by the instrument level-1 noise and spectral fit quality by limiting the contributions from other components such as anthropogenically pollution sources. Figure 3.1.1 shows a temporal evolution of the statistical NO2 slant column uncertainties from the AC-SAF GOME-2A (2007-2021), GOME-2B (2013-2022), and GOME-2C (2019-2022). All three GOME-2 instruments show a positive trend due to the propagation of measurement noise over time. For GOME-2A, a relatively fast increase rate of NO_2 slant column uncertainties by 5.2 % yr^{-1} is found until the second throughput test in September 2009. The second throughput test, which initially resulted in an additional loss of signal-to-noise, has positive effects on the quality of the level-1 data by weakening the long-term drift of the instrument's slit function. Therefore, following the test, GOME-2A NO_2 slant column uncertainties increase at a slower pace of 1.8% yr^{-1} until 2019. From 2020 until its lifespan, the quality of GOME-2A NO_2 fits deteriorated rapidly due to a fast degradation of level-1 data, resulting in a sharp increase in NO_2 slant column uncertainties at a rate of 17.5% yr^{-1}. The AC-SAF GOME-2B shows a comparable but slightly lower increase rate in NO_2 slant column uncertainties (1.2% yr^{-1}) over the 10-year period from 2013 to 2022 when compared with GOME-2A, due to their identical spectral retrieval settings. In contrast, GOME-2C has a relatively higher trend of increase in NO_2 slant column uncertainties during its initial phase of operation compared to GOME-2A and GOME-2B. This trend may be attributed to a combination of factors, including detector degradation and differences in spectral fit settings for GOME-2C in the AC-SAF algorithm.

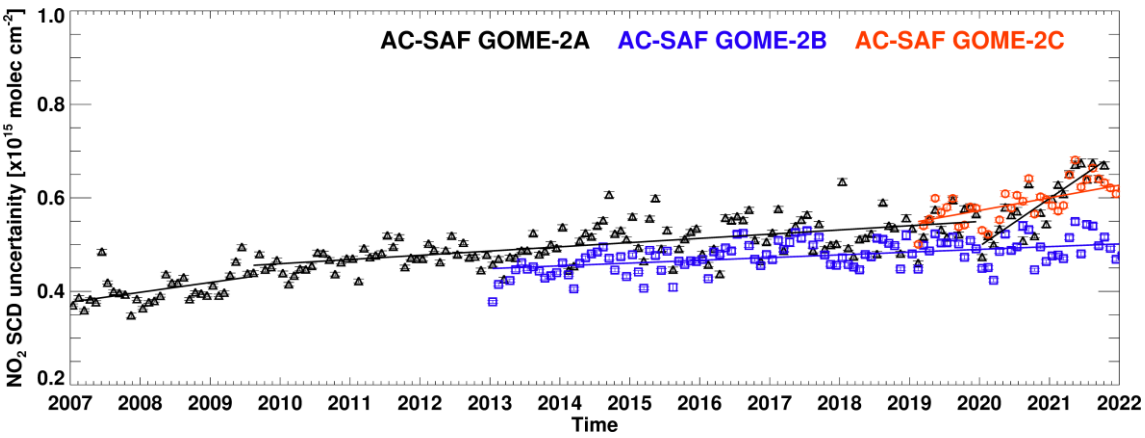

Figure 3.1.1. Temporal evolution of the statistical NO_2 slant column uncertainties from GOME-2 on MetOp-A/B/C retrieved from the AC-SAF algorithm. These uncertainties are calculated using the slant column retrievals over the clean Pacific region on day 15 of each month. Solid lines represent the linear regressions fitted for each instrument's periods. Error bars indicate one standard deviation (1σ).

Figure 3.1.2 below shows the evolution of the TROPOMI NO_2 slant column statistical uncertainty over time. The red line shows a 21-day running mean. Between 1 August 2019 and 1 July 2023 the TROPOMI NO_2 SCD statistical uncertainty has increased by 6%, corresponding to a trend of 1.5 % yr^{-1}. The result is an update of the material presented in van Geffen et al. (2022).

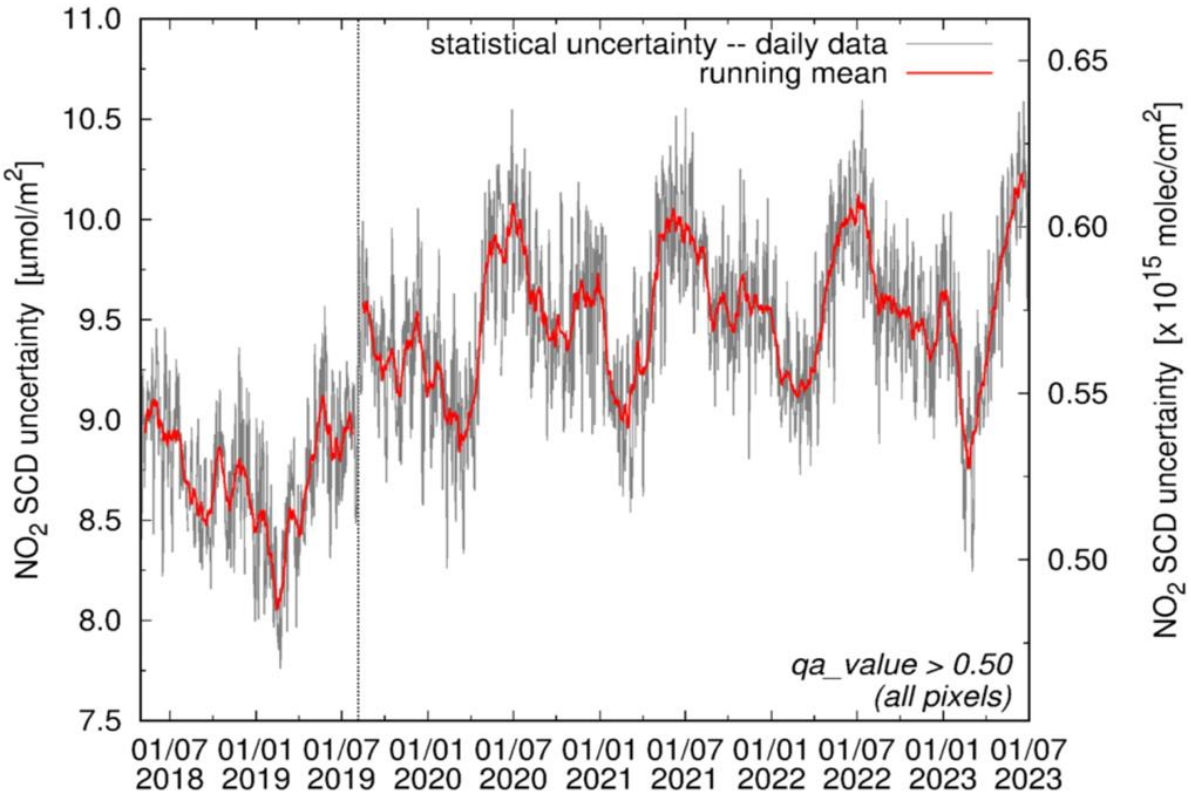

Figure 3.1.2 Statistical uncertainty in TROPOMI NO_2 slant columns as a function of time. The thin vertical grey line indicates the day that the along-track size of the TROPOMI pixel was reduced, which resulted in smaller pixels and therefore larger per-pixel uncertainties.

Nevertheless, there are also known systematic effects, such as the choice to include or omit a term describing the I_0-offset in the NO_2 spectral fitting. Earlier work by Oldeman (2018) has showed that including the I_0-correction leads to 1×10^{15} molec. cm^{-2} smaller TROPOMI NO_2 SCDs and up to 0-30% (average: 8%) lower NO_2 SCD uncertainties for clear-sky ocean scenes but has a near-zero effect over land and over cloudy scenes. Since some of the spectral fitting approaches include the I_0-correction (GOME, SCIAMACHY, GOME-2), but others do not, we should account for a systematic uncertainty of 1×10^{15} molec. cm^{-2}.

3.1.3. NO_2 stratospheric correction uncertainty estimate

Stratospheric NO_2 columns and associated tropospheric residuals can be estimated with different approaches. The KNMI data assimilation approach, applied in the QA4ECV (Boersma et al., 2018) and the operational OMI and TROPOMI retrieval algorithms, and the STREAM

scheme, used by DLR for AC-SAF retrievals provide more insight into the NO2 stratospheric correction uncertainties.

The theoretical uncertainty estimates for the data assimilation (derived from observation minus forecast statistics of the assimilation scheme, Dirksen et al. (2018)) and for STREAM are both on the order of 0.2×10^{15} molec. cm^{-2} (Beirle et al., 2016). Comparisons in the Round Robin indicate that, on a day-to-day basis, the differences between the stratospheric NO_2 columns from data assimilation and STREAM were generally smaller than 0.5×10^{15} molec. cm^{-2} which can be considered an upper limit of the systematic uncertainty in the stratospheric NO_2 estimate. There is generally good agreement in spatiotemporal variability in stratospheric NO_2 between data assimilation and STREAM. STREAM, with the settings used by DLR, attributes generally a higher fraction of the NO_2 SCDs to stratospheric NO_2, so that tropospheric NO_2 columns retrieved with data assimilation are higher by up to 1×10^{15} molec. cm^{-2}, and tropospheric NO_2 columns retrieved with STREAM can be occasionally negative.

Table 3.1.2 summarizes the random and systematic uncertainties which have been investigated specifically for GOME-2A (in the ESA CCI ECV Precursor project and Liu et al. (2019)), for OMI (in QA4ECV), and for TROPOMI (in the S5P project). Those studies gave very similar conclusions, so we hold the uncertainty estimates representative for all sensors and both the data assimilation and STREAM methods studied here.

Table 3.1.2 NO_2 stratospheric slant column (statistical) uncertainties (typical, per pixel).

	$\sigma_{N_{s,strat}}$ (random)	$\sigma_{N_{s,strat}}$ (systematic)
All sensors	0.2×10^{15} molec. cm^{-2}	$<0.5\times10^{15}$ molec. cm^{-2}

3.1.4. Tropospheric air mass factor uncertainty estimates

The theoretical uncertainties in the tropospheric AMF are calculated with Eq. (3.1.3), which, for every pixel, accounts for the sensitivity of the AMF to changes in the local forward model parameter value, evaluated around the specific value for the parameter at that pixel. The uncertainties in the surface albedo, surface pressure height, cloud fraction, cloud pressure are estimated from the literature, or estimated from intercomparisons with independent data. Typical values in the NO_2 AMF calculation are σ_{A_s}=0.015, $\sigma_{f_{cl}}$=0.025, $\sigma_{p_{cl}}$ =50 hPa. Because the retrieved cloud paramaters generally depend on (or are reasonably consistent with) the same assumed surface albedo as used for the AMF calculation, AMF uncertainties related to clouds and surface albedo will be dampened (Boersma et al. (2004); Boersma et al. (2018)).

AMF uncertainties due uncertainties in the cloud fraction and cloud pressure are 5%-10% in magnitude (Boersma et al., 2018), although they can be much larger when the cloud retrieval algorithm suffers from systematic errors such as in the early TROPOMI mission phase, when cloud pressures were biased low before FRESCO+ wide was implemented (Riess et al. (2022); van Geffen et al. (2022)). AMF uncertainties due to uncertainties in surface albedo are 10%. AMF uncertainties from NO_2 profile uncertainty are 10%-30%, based on the Round Robin comparison of tropospheric AMFs calculated with profiles from either TM5-MP or CAMS for

strongly polluted regions (10%) and regions with enhanced background NO_2 (30%). Recent work from Douros et al. (2023) suggests that for TROPOMI, with its high resolution, the 10% profile uncertainty should probably be increased to 20% for polluted situations, reflecting the strong variability and heterogeneity in NO_2 profiles at the size of a TROPOMI pixel (3.5×5.5 km^2).

Table 3.1.3 provide a general estimate of the AMF uncertainties that are expected in the tropospheric NO_2 retrievals under polluted conditions. In such situations, the AMF uncertainty dominates the overall uncertainty budget. Aerosol-related uncertainties are not explicitly accounted for in the uncertainty analysis, because cloud retrievals are sensitive to scattering aerosols that prevail over many polluted regions, and effectively account for aerosol effects in the AMF calculation (Boersma et al., 2004; Boersma et al. 2011). It is known that for situations with strongly absorbing aerosols, the cloud retrievals do not capture the effect of aerosols, and substantial errors can occur (Castellanos et al. (2015); Liu et al. (2019;2020)). In a general sense, the effect of scattering aerosols on AMF calculations dominates over the effect of absorbing aerosols, whose impact is episodically significant over biomass burning regions, deserts, and some industrial hotspots (e.g. Sand et al., 2021).

Table 3.1.3 Contributions to the tropospheric AMF uncertainty due to various contributions. Especially the contribution from the a priori NO_2 profile uncertainty will be larger for the high-resolution sensors OMI and especially TROPOMI.

	Uncertainty in model parameter	Corrresponding contribution to $\sigma_{M_{tr}}/M_{tr}$
Surface albedo	σ_{A_s}=0.015	±10%
Cloud fraction	$\sigma_{f_{cl}}$=0.025	5-10%
Cloud pressure	$\sigma_{p_{cl}}$ =50 hPa	5-10%
A priori NO_2 profile shape		10-30% (sensor dependent)
Overall AMF uncertainty ($\sigma_{M_{tr}}$)		20-35% (sensor dependent)

3.1.5. Overall NO_2 retrieval uncertainties

The overall uncertainty in the tropospheric columns is driven by the propagation of uncertainties via Eq. (3.1.2). The overall uncertainty depends on the details of the individual retrieval and therefore differs from one pixel to the next. For small tropospheric NO_2 columns, such as over pristine or background areas, the overall uncertainty is dominated by the uncertainty from the spectral fitting process, whereas over polluted regions with high tropospheric NO_2 columns, the retrieval uncertainty is dominated by the AMF uncertainty.

Table 3.1.4 summarizes the assessment of the main contributions to the overall uncertainty budget for tropospheric NO_2 retrievals. These uncertainties should be interpreted as representative of typical single-pixel uncertainties for retrievals over polluted regions

encountered by users. Expressions for systematic or structural uncertainty are under investigation and will be provided in cycle 2 of the project.

Table 3.1.4 Estimation of the uncertainty contributions to the overall, per-pixel tropospheric NO_2 column uncertainty over polluted regions.

Uncertainty contribution	Random	Systematic
From NO_2 slant column ($\frac{\sigma_{N_S}}{M_{tr}}$)	0.4-0.8×10^{15} molec. cm^{-2}	< 1.0×10^{15} molec. cm^{-2}
From stratosphere ($\frac{\sigma_{N_{S,strat}}}{M_{tr}}$)	0.2×10^{15} molec. cm^{-2}	< 0.5×10^{15} molec. cm^{-2}
From tropospheric AMF ($\frac{\sigma_{N_S}}{M_{tr}}$)	20-35% (sensor dependent)	TBD
Approximation for σ_{N_v}	$\sigma_{N_v} = 0.5 \times 10^{15} + 0.3N_v$	TBD

3.2. Formaldehyde (L2-HCHO)

3.2.1. Uncertainty propagation

The tropospheric HCHO vertical column density is retrieved with the following equation:

$$N_v = \frac{N_s - \overline{N_{s,0}}}{M} + \overline{N_{v,0}} \tag{3.2-1}$$

A formulation of the uncertainty can be derived analytically by error propagation, starting from the equation of the vertical column (Eq. (**3.2-1**) which directly results from the different retrieval steps. If we assume normal probability distributions, the total uncertainty on the tropospheric vertical column can be expressed as [Boersma et al., 2004, De Smedt et al., 2018]:

$$\sigma_{N,v}{}^2 = \left(\frac{\partial N_v}{\partial N_s}\sigma_{N,s}\right)^2 + \left(\frac{\partial N_v}{\partial M}\sigma_M\right)^2 + \left(\frac{\partial N_v}{\partial N_{v,0}}\sigma_{N,v,0}\right)^2 \tag{3.2-2}$$

$$\sigma_{N,v}{}^2 = \frac{1}{M^2}\left(\sigma_{N,s}{}^2 + \frac{\Delta N_S{}^2}{M^2}\sigma_M{}^2\right) + \sigma_{N,v,0}{}^2 \tag{3.2-3}$$

where $\sigma_{N,s}$, σ_M, and $\sigma_{N,v,0}$ are respectively the errors on the slant column, the air mass factor, and the background vertical column in the reference sector (indicated by suffix 0).

For each of these three categories, more details on the implementation of the uncertainty values in the L2 algorithm can be found in the TROPOMI HCHO ATDB (De Smedt et al., 2018). A summary of the sources of uncertainties and their estimated size are presented the next sections.

3.2.2. Retrieval uncertainty characterisation: systematic and random components

In principle, systematic and random components of each given error source should be discriminated. If so, when deriving the error on any average of HCHO vertical columns, each of the components of Eq. ((3.2-2) can be written as:

$$\sigma_k^2 = \frac{\sigma_{k,rand}^2}{N} + \sigma_{k,syst}^2 \tag{3.2-4}$$

where N is the number of ground pixels considered when averaging the observations. It is however very difficult to separate random and systematic contributions. Our approach is to qualify an error contribution as “random” if its impact on the column tends to average out in space and time. Typically, the uncertainty of the slant columns is of random type. Any other error contribution will be qualified as “systematic”.

The GCOS spatial and temporal threshold requirements for HCHO are respectively 100 km and 1 month. See Figure 3.2-2 for the estimated precision of OMI and TROPOMI HCHO columns at different spatial and temporal scales.

3.2.3. HCHO slant column density uncertainty estimates

The random uncertainty of the HCHO slant columns is estimated based on the slant column errors of the DOAS fits, and on the standard deviations of the slant columns in the remote Equatorial Pacific (as illustrated on Figure 3.2-1 and summarized in Table 3.2-1 for each sensor). To this random component, we consider an additional systematic error of 20% of the background-corrected slant columns.

Table 3.2-1 HCHO slant column random uncertainties (typical, per pixel) recently estimated in the QA4ECV, S5P, and ECV Precursor projects.

	$\sigma_{N,s,rand}$	Reference
GOME	2.7×10^{15} molec.cm^{-2}	Zara et al., 2018 De Smedt et al., 2015, 2018, 2021.
SCIAMACHY	$6\text{-}8\times10^{15}$ molec.cm^{-2}	
GOME-2	$7\text{-}13\times10^{15}$ molec.cm^{-2}	
OMI	8×10^{15} molec.cm^{-2}	
TROPOMI	$6\text{-}7\times10^{15}$ molec.cm^{-2}	

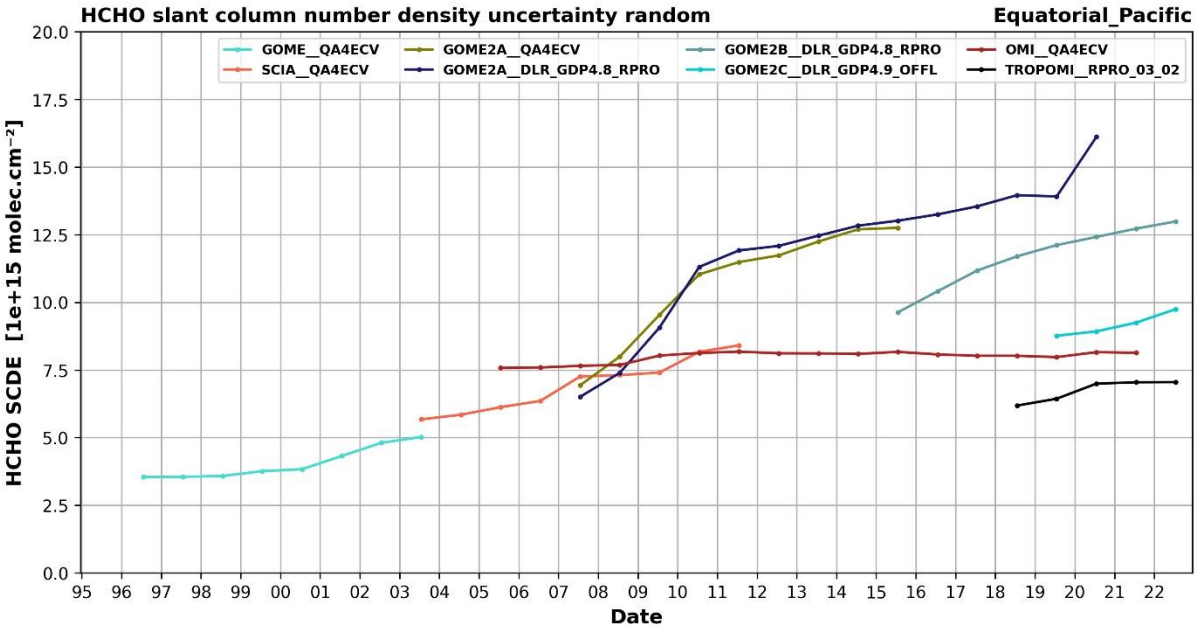

Figure 3.2-1 Annual average of the HCHO slant column random uncertainty in the Equatorial Pacific region.

3.2.4. Tropospheric air mass factor uncertainty estimates

The uncertainties on the air mass factor depend on input parameter uncertainties and on the sensitivity of the air mass factor to each of them. This contribution is broken down into the squared sum [Boersma et al., 2004, De Smedt et al., 2018]:

$$\sigma_M{}^2 = \left(\frac{\partial M}{\partial A_s}\cdot\sigma_{A,s}\right)^2 + \left(\frac{\partial M}{\partial f_c}\cdot\sigma_{f,c}\right)^2 + \left(\frac{\partial M}{\partial p_{cloud}}\cdot\sigma_{p,cloud}\right)^2 + \left(\frac{\partial M}{\partial s}\cdot\sigma_s\right)^2 + (0.15M)^2 \quad (3.2\text{-}5)$$

The contribution of each parameter to the total air mass factor uncertainty depends on the observation conditions. The air mass factor sensitivities ($M' = \frac{\partial M}{\partial parameter}$), i.e. the air mass factor derivatives with respect to the different input parameters, can be derived for any particular condition of observation using the altitude-dependent AMF LUT, and using the model profile shapes. It should be stressed that the uncertainty on the profile shape is estimated using one parameter describing the shape of the profile: the profile height, i.e., the pressure below which resides 75% of the integrated HCHO profile. The errors $\sigma_{A,s}, \sigma_{f,c}, \sigma_{p,cloud}, \sigma_{s,h}$ are typical uncertainties on the surface albedo, cloud fraction, cloud pressure and profile shape, respectively. The fifth term on the right of Eq. ((**3.2-5**) represents the structural uncertainty contribution due to possible errors in the AMF model itself (Lorente et al., 2017). We estimate this contribution to 15% of the air mass factor.

Estimates of the air mass factor errors and of their impact on the vertical column uncertainties are listed in Table 3.2-2. They are based on the application of equation (**3.2-5** to HCHO columns retrieved from OMI and TROPOMI measurements.

Table 3.2-2 Summary of the different error sources considered in the air mass factor error budget.

Error source	Type	Parameter uncertainty	Estimated uncertainty on HCHO VCD
Surface albedo	systematic	0.02	10%
Cloud fraction	random	0.05	10%
Cloud height	random	50hPa	20%
Profile shape height	systematic	100hPa	30-60%
Structural uncertainty	systematic	15%	5-15%

3.2.5. Background correction uncertainty estimates

This error includes contributions from the model background vertical column, from the error on the air mass factor in the reference sector, and from the amplitude of the normalization applied to the HCHO columns. The uncertainty on the air mass factor in the reference sector is calculated as in Eq. ((**3.2-5**) and saved during the background correction step. Uncertainty on the model background has been estimated as the monthly averaged differences between two different CTM simulations in the reference sector: IMAGES (Stavrakou et al., 2009a) and TM5 (Huijnen et al., 2010).

Table 3.2-3 Estimated errors on the reference sector correction.

Error source	Type	Uncertainty on HCHO VCD	Evaluation method – reference
Model background	systematic	0.5-1.5x10^{15} molec.cm^{-2}	Difference between IMAGES and TM5 model
Amplitude of the column normalisation	systematic	0-4x10^{15} molec.cm^{-2}	Sensitivity tests using GOME-2 and OMI data.

3.2.6. Overall HCHO retrieval uncertainties

Here are presented respectively our current estimates of the precision (random error uncertainty) and the trueness (systematic error uncertainty) of the HCHO vertical columns. These estimates are mainly based on OMI and TROPOMI HCHO retrievals.

Precision

The precision of the slant columns is provided in Table 3.2-1 on an individual pixel basis and for each sensor. In the case of HCHO, this source of uncertainty will dominate the final vertical column precision. The precision can be improved by averaging the data. At a given spatio-

temporal resolution, the precision will depend on the initial SCD precision and on the number of observations included in the average (sensor dependent).

Figure 3.2-2 shows the estimated precision of OMI and TROPOMI HCHO columns at different spatial and temporal scales, for continental emissions and in the remote reference sector (from De Smedt et al., 2021). The theoretical noise corresponds to single-measurement precision divided by the square root of observations. The horizontal blue line at $1.3x10^{15}$ molec.cm^{-2} represents the Copernicus user requirement. TROPOMI significantly improves the precision of the HCHO observations at short temporal scales and for low HCHO columns. Compared to OMI, the precision of the TROPOMI HCHO columns is improved by 25 % for individual pixels and by up to a factor of 3 when considering daily averages in 20 km radius circles.

Trueness

Table 3.2-4 provides estimates of the systematic uncertainty on the HCHO tropospheric columns, for two different NMVOC emission regimes (low/high HCHO columns). This evaluation was made for the QA4ECV project, based on OMI data. More recent validation studies based on TROPOMI data agree with those estimates (Vigouroux et al., 2020, De Smedt et al., 2021). The largest contribution to the systematic uncertainty on the vertical columns comes from air mass factor uncertainty and is mainly related to the auxiliary data used in the AMF calculation. Therefore, we do not expect large differences between the different sensors. The largest contribution is from the a priori profile uncertainty. In the case where the satellite averaging kernels are used for comparisons with external HCHO columns, the a priori profile contribution can be removed from the relative comparison uncertainty budget, leading to a total uncertainty in the range of 25% to 50%.

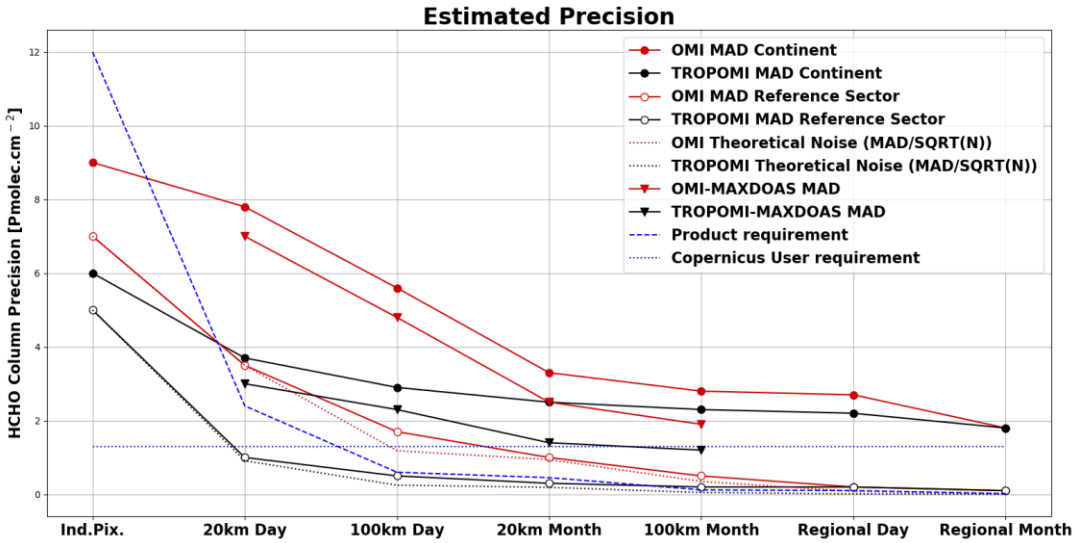

Figure 3.2-2 Estimated precision of OMI (in red) and TROPOMI (in black) HCHO columns at different spatial and temporal scales (20km, 100km, regions, day/month) (from De Smedt et al., 2021). The median deviation of the satellite HCHO columns are provided for continental emissions (plain circles)

and in the remote reference sector (white circles). Validation estimates are plotted at 20km and 100km (MAD of differences between satellite and MAX-DOAS columns, triangles). The theoretical noise (dotted lines) corresponds to single measurement precision divided by the square root of observations. The dashed blue line is the TROPOMI product requirement, based on a single measurement precision of $12x10^{15}$ molec.cm^{-2}. The horizontal blue line at $1.3x10^{15}$ molec.cm^{-2} represents the COPERNICUS user requirement. [Pmolec.cm^{-2} = $1x10^{15}$ molec.cm^{-2}].

Table 3.2-4: Estimated HCHO vertical column uncertainty budget for monthly averaged low and elevated columns (higher than $1x10^{16}$ molec.cm^{-2}). Contributions from the three retrieval steps are provided, as well as input parameter contributions.

HCHO vertical error uncertainty	Remote regions / low columns	Elevated column regions / periods
Contribution from systematic slant columns uncertainties	25%	15%
Contribution from air mass factors uncertainties	75%	30%
• from a priori profile errors • from model errors • from albedo errors • from cloud top pressure errors • from cloud fraction errors	• 60% • 35% • 20% • 20% • 15%	• 30% • 15% • 10% • 10% • 05%
Contribution from background correction uncertainties	40%	10%
Total	**90%**	**35%**
Total without smoothing error	**50%**	**25%**

3.3. Sulfur dioxide (L2-SO2)

3.3.1. Uncertainty propagation

The total uncertainty (accuracy and precision) on the SO_2 columns produced by the algorithm, it is composed of many sources of error (see e.g., Theys et al., 2017). Several of them are related to the instrument and propagate into the uncertainty on the slant column. Other types of error can be considered as forward model errors and are related to the representation of the physics in the algorithm and can affect the slant column results or the air mass factors.
Another important point is that one should differentiate systematic and random components of a given error source V:

$$\sigma_V^2 = \frac{\sigma_{V(rand)}^2}{n} + \sigma_{V(syst)}^2 \qquad (3.3\text{-}1)$$

here *n* is the number of pixels considered. However, these are hard to separate in practice. Therefore, error contributions are (tentatively) classified as either “random” or “systematic” errors, depending on their tendencies to average out in space/time or not. These error estimates are labelled as “precison” and “trueness” in the TROPOMI data files.

As a matter of fact, the total retrieval uncertainty on the SO_2 vertical columns can be derived by propagation of errors from the two indepent retrieval steps:

$$\sigma_{N_v}^2 = (\frac{\sigma_{N_S}}{M})^2 + (N_v.\frac{\sigma_M}{M})^2 \quad (3.3\text{-}2)$$

where $\sigma_{VCD}, \sigma_{SCD}, \sigma_{AMF}$ are the errors on the vertical column, slant column and air mass factor, respectively. The AMF error can be broken down into a squared sum of terms (Boersma et al., 2004):

$$\sigma_M^2 = \left(\frac{\partial M}{\partial A_s} \cdot \sigma_{\text{alb}}\right)^2 + \left(\frac{\partial M}{\partial p_{cl}} \cdot \sigma_{\text{ctp}}\right)^2 + \left(\frac{\partial M}{\partial f_{cl}} \cdot \sigma_{feff}\right)^2 + \left(\frac{\partial M}{\partial s} \cdot \sigma_s\right)^2 \quad (3.3\text{-}3)$$

where σ_{As}, σ_{pcl}, σ_{fcl}, σ_s are typical uncertainties on the albedo, cloud top pressure, cloud fraction and profile shape, respectively.
The contribution of each parameter to the total air mass factor error depends on the observation conditions. The air mass factor sensitivities ($\frac{\partial M}{\partial parameter}$), i.e., the air mass factor derivatives with respect to the different input parameters, can be derived for any condition of observation using the altitude-dependent AMF LUT and using the a-priori profile shapes. It should be stressed that the uncertainty on the profile shape is estimated using one parameter describing the shape of the profile: the profile height, i.e., the pressure below which resides 75% of the integrated SO2 profile.

Note that this error analysis is complemented by the total column averaging kernel (AK) as described in Eskes and Boersma (2003):

$$AK(p) = \frac{m'(p)}{M} \quad (3.3\text{-}4)$$

(m' is the weighting function, Eq. 3.6 in the ATBD SO_2 part) which characterizes the sensitivity of the retrieved column to a change in the true profile. For certain applications, the AK is particulary useful to apply an apriori substitution using another SO_2 profile. In that case, the systematic uncertainty on the AMF due to the uncertainty on the profile is zero, and it is recommended to use in the output files the "trueness_kernel" field, that leaves out the profile error from the AMF error calculation.

3.3.2. SO_2 slant column density uncertainty estimates

Error sources that contribute to the total uncertainty on the slant column originate both from instrument characteristics and uncertainties/limitations in the COBRA slant column fitting algorithm. A summary is given in Table 3.3.1, at low/high SZA (latitudes). For the random component of the slant column errors, the error on the slant columns provided by the COBRA fit is considered (referred as SCDE) as it is assumed to be dominated by and representative of the different random sources of error.

For the systematic errors on the slant column, the numbers provided in Table 3.3.1 have been determined based on sensitivity tests and based on the actual data. For instance, systematic

SCD offsets are sometimes found over clean areas, and are accounted for in Table 3.3.1 in the form of an absolute term. The relative term accounts for the uncertainty on the SO_2 cross-section and other spectral interferences.

Table 3.3.1 SO_2 slant column uncertainties (typical, per pixel) recently estimated in the S5P and ECV Precursor projects. Note: 1DU=1 Dobson unit (1DU: 2.69 x 10^{16} molecules/cm²).

	σ_{NS} (SZA=30°/60°)	Reference
GOME	Random: 0.15 DU /0.3 DU Systematic: 0.05 DU + 10% /0.1 + 15%	-
SCIAMACHY	tbd	-
OMI	Random: 0.2 DU /0.4 DU Systematic: 0.05 DU + 10% /0.1 + 15%	-
TROPOMI	Random: 0.2 DU /0.4 DU Systematic: 0.05 DU + 10% /0.1 + 15%	Theys et al. (2017, 2021)

3.3.3. Tropospheric air mass factor uncertainty estimates

For SO_2, the main error source is related to the air mass factor, as it depends on many input parameters that are not always well constrained. Using Eq. 3.3.3, one can calculate a total AMF error based on typical uncertainties on the input parameters. Here we use fixed values set to σ_{As}=0.02, σ_{pcl}=50 hPa, σ_{fcl}=0.05, σ_s=75 hPa. The resulting uncertainty budget is based on the error analysis from the TROPOMI SO_2 retrieval algorithm (Theys et al., 2017), but is also consolidated with results from the CCI+precursors round Robin SO_2 exercise.

Generally speaking, it is difficult to ascertain whether a source of error is purely random or systemacic. Several sources have the tendency to reduce by spatial or temporal averaging and are labelled as 'random'. Conversely, other error sources that do not average out are classified as 'systematic'.

Errors due to uncertainties on cloud fraction and cloud pressure are typically random errors, and account for 5% and 20% on the VCDs, respectively. Inversely, applying a cloud correction to the AMF or not, has a systematic effect of about 10% on the VCDs.

Errors due to uncertainties on the surface albedo is of ~15% (systematic), while the SO2 profile shape related error ranges from 20-50% and is considered as the largest systematic error source. However, for some applications, this error can be mitigated by using the column averaging kernels (see section 3.3.1).

Finally, additional systematic errors are due to the effect of atmospheric aerosols on the measurement sensitivity (15-25%) and other forward model errors (structural errors ~15%).

3.3.4. Overall SO_2 retrieval uncertainties

Table 3.3.2 summarizes the assessment of the main contributions to the global error budget on SO_2 retrieval from COBRA.

Table 3.3.2 Estimation of the error sources of the SO_2 COBRA retrieval (preliminary) for typical polluted conditions, at low/high SZA (latitudes). Blue and red fields indicate random (precision) and systematic (trueness) errors. Total errors are computed assuming all contributions are mutually uncorrelated.

Error source	Error on VCD	
	SZA=30°	SZA=60°
Instrument signal-to-noise	0.6 DU	1.2 DU
SO_2 absorption cross-section, spectral interferences +instrumental features	0.1 DU + 10%	0.2 DU + 15%
Surface albedo*	15%	15%
SO_2 Profile shape	20-50%	20-50%
Cloud correction	10%	10%
Cloud fraction	5%	5%
Cloud pressure	20%	20%
Aerosols (except in case of volcanic eruptions)	< 15%	< 25%
Structural (AMF)	15%	15%
Total random error	0.6 DU + 20%	1.2 DU + 20%
Total systematic error	0.1 DU + 45%	0.2 DU + 55 %
Total systematic error kernel	0.1 DU + 27%	0.2 DU + 35 %

*snow/ice free scenes

3.4. Glyoxal (L2-CHOCHO)

3.4.1. Uncertainty propagation

The total uncertainty on the retrieved glyoxal tropospheric columns is determined by many different factors, including instrument noise, radiative transfer modelling errors, errors in the absorption cross sections, or uncertainty in a priori information. We provide an overview of the different sources of uncertainty and estimate their contribution, as described in Lerot at al. (2021).

Following (Boersma et al., 2004; Lerot et al., 2010; De Smedt et al., 2008), the total error on the retrieved vertical column N_V can be expressed as:

$$\sigma_{N_V}^2 = \frac{1}{M^2}\left({\sigma_{N_s}}^2 + \boldsymbol{N_V^2}\,{\sigma_M}^2 + {\sigma_{N_{s,0}}}^2 + {N_{v,0,ref}}^2{\sigma_{M,0}}^2 + {M_0}^2{\sigma^2}_{N_{v,0,ref}}\right) \quad (3.4\text{-}1)$$

where σ_{N_s}, σ_M and $\sigma_{N_{v,0,ref}}$ are the errors on the slant column, the air mass factor and the reference value used in the background correction, respectively. $\sigma_{N_{s,0}}$ and $\sigma_{M,0}$ represent the

errors on the slant column and air mass factor for pixels belonging to the reference Pacific sector used for the background correction. The three last terms together represent the error associated to the background correction.

We distinguish random errors, which tend to zero when averaging observations, from systematic errors, which are correlated in time and/or space. However, it is difficult to make this distinction in practice, as the various systematic error components have different correlation lengths and timescales (Boersma et al., 2004). For the glyoxal error budget, we consider the propagation of the instrumental shot noise in the slant column retrieval as the main random error. For weak absorbers such glyoxal, this error component dominates for individual measurements and depends on the observation geometry, the scene reflectivity, and on the instrument itself. The other error components are treated as systematic, though this assumption may lead to conservative systematic error estimates and to an underestimation of the product scatter, depending on the time and spatial resolution of interest. Specifically, uncertainties associated to the input parameters needed for the AMF calculation are directly related to the resolution of the used databases and may appear as random at coarser resolution. This has been discussed by Vigouroux et al. (2020) who attributed part of the scatter in formaldehyde vertical column TROPOMI/MAX-DOAS differences to a random component of the AMF errors.

The following sections discuss the different error components in detail.

3.4.2. Slant column errors

The retrieval noise for individual observations is limited by the instrument signal-to-noise ratio. The corresponding random errors on the slant column retrieval is estimated using the root mean square optical depth residual and the covariance matrix of the linear fit (Danckaert et al., 2017).

There are also systematic errors associated to the DOAS spectral fit, that are mainly dominated by slit function and wavelength calibration uncertainties, absorption cross-section uncertainties, by interferences with other species (O_4, liquid water, Ring, …), or by stray light corrections. Those contributions to the slant column errors are difficult to assess and can only be approximated from sensitivity tests (Lerot et al., 2010). In general, this term can be as high as 2–3×10^{14} molec.cm^{-2}. However, the use of a radiance as the DOAS fit reference and the application of the background correction removes a large part of the systematic error in the slant column fit. Therefore, we pragmatically estimate this remaining systematic slant column error $\sigma_{N_{s,syst}}$ to 1×10^{14} molec.cm^{-2}.

3.4.3. Air mass factor errors

The errors on the air mass factor depend on input parameter uncertainties and on the sensitivity of the air mass factor to each of them. This contribution is broken down into the squared sum (Boersma et al., 2004; Lerot et al., 2010; De Smedt et al., 2008):

$$\sigma_{M,syst}^2 = \left(\frac{\partial M}{\partial A_s} \cdot \sigma_{A_s}\right)^2 + \left(\frac{\partial M}{\partial s} \cdot \sigma_s\right)^2 + (0.15M)^2 \quad (3.4\text{-}2)$$

where σ_{A_s}, σ_s are typical uncertainties on the surface albedo and profile shape, respectively. They are estimated from the literature or derived from comparisons with independent data. The contribution of each parameter to the total air mass factor error depends on the observation conditions. The air mass factor sensitivities ($M' = \frac{\partial M}{\partial parameter}$), i.e. the air mass factor derivatives with respect to the different input parameters, can be derived for any particular condition of observation using the altitude-dependent AMF LUT, created with VLIDORT, and using the model profile shapes. In practice, a LUT of AMF sensitivities has been created using reduced grids from the AMF LUT and a parameterisation of the profile shapes.

A reasonable uncertainty on the albedo is $\sigma_{A_s} = 0.02$ (Kleipool et al., 2008). Using this value and the AMF sensitivity LUT allows to estimate for every pixel the first term of Eq. (3.4.2) and gives the AMF error component related to the surface reflectivity. Of course, in practice, more substantial errors can be introduced if the real albedo differs considerably from what is expected, for example in the case of the sudden snowfall or ice cover.

The uncertainty associated to the a priori profile shapes (the smoothing error) used in the retrieval are more difficult to assess, especially due to the scarcity of independent glyoxal profile measurements. Those errors are nevertheless large owing to the large uncertainty in our current knowledge of the glyoxal production mechanisms. To assess this error component and the sensitivity of the air mass factor to the profile shape, we have introduced one profile effective pressure s_p, i.e. the pressure below which resides 50% of the integrated glyoxal profile. $\frac{\partial M}{\partial s}$ is approximated by $\frac{\partial M}{\partial s_p}$ and σ_s is taken equal to 50hPa. The latter value corresponds to the typical standard deviation of the model profile shape effective heights over polluted regions. Note that the error related to the a priori profiles can be removed with the use of the averaging kernels when comparing the satellite glyoxal columns to independent glyoxal profile measurements from models or MAX-DOAS. That is the reason why an estimate of the total systematic error without this smoothing error is also provided in the L2 product:

$$\sigma_{M,syst,kernel}^2 = \left(\frac{\partial M}{\partial A_s} \cdot \sigma_{A_s}\right)^2 + (0.15M)^2 \quad (3.4\text{-}3)$$

The third term in Eq. (3.4.2) accounts for possible error in the AMF model itself (e.g. wavelength dependence, neglect of aerosols,…) and is estimated to be 15% of the air mass factor (Lorente et al., 2017).

As explained in the CCI+ precursors ATBD, no cloud correction is applied to compute the AMFs. Therefore, it is highly recommended to apply a stringent filter based on the cloud fraction

(<20%) on the retrieved glyoxal vertical columns. Nevertheless, even with such a filter, an error on the AMF caused by residual cloud contamination may remain. This error, which strongly depends on the cloud coverage and altitude, is expected to average out in space and/or time when combining several observations. To consider this, we add a small random contribution to the air mass factor as:

$$\sigma_{M,rand}^2 = (0.05M)^2 \quad (3.4\text{-}4)$$

The designed spatial and temporal threshold requirements for CHOCHO are respectively 100km and 1 month. See table 3.4.1 for the typical CHOCHO VCD precision estimates.

3.4.4. Background correction error

Although the background correction is designed to overcome systematic features/deficiencies of the slant column fitting, some errors are also associated to this procedure. In particular, systematic errors on the reference slant columns and their air mass factors are propagated to the computed correction values. Also, there is an uncertainty related to the used reference value of the glyoxal vertical column in the reference sector $N_{v,0,ref}$. Considering these different components, the background correction error can be estimated as:

$$\sigma_{bck}^2 = \frac{1}{M^2}\left({\sigma_{N_{s,0}}}^2 + {N_{v,0,ref}}^2{\sigma_{M,0}}^2 + {M_0}^2{\sigma_{N_{v,0,ref}}}^2\right) \quad (3.4\text{-}5)$$

where $\sigma_{N_{s,0}}$ is the systematic slant column error fixed to 1x10^{14} molec/cm² (see section 3.4.2), M_0 and $\sigma_{M,0}$ are the air mass factors and associated systematic errors in the background correction reference sector. $\sigma_{N_{v,0,ref}}$ represents the error associated to the reference vertical column density $N_{v,0,ref}$ and is fixed to 5x10^{13} molec/cm².

3.4.5. Global budget: Total precision and trueness

Combining the different error components discussed above, the total random error (or precision) is computed as

$$\sigma_{Nv,rand}^2 = \frac{\sigma_{Ns,rand}^2 + \sigma_{M,rand}^2 N_v^2}{M^2} \quad (3.4\text{-}6)$$

Table 3.4.1 provides typical values for each instrument.

The instrumental signal-to-noise ratio is the main factor introducing random errors in the product. The TROPOMI instrument has a signal-to-noise ratio around 1600 in the visible spectral range for low albedo scenes. Figure 3.4.1 illustrates the glyoxal VCD random error estimates for one day of TROPOMI observations (1st June 2018). This random error is generally less than 0.8-1x10^{15} molec/cm² over dark surfaces and much lower for bright surfaces (clouds

and snow-covered scenes). Previous studies (Alvarado et al., 2014; Chan Miller et al., 2014; Lerot et al., 2010) have shown that this random error is slightly larger for the older instruments GOME-2 and OMI (in the range 1-1.5 x 10^{15} molec/cm²). For individual satellite ground pixels, the random error is the dominant source of error on the total vertical column. This clearly points to the importance of the spatial/temporal averages, which reduce the random error by the square root of the number of observations and facilitate the detection of meaningful glyoxal signal.

Table 3.4.1 Typical CHOCHO VCD precision estimates (Lerot et al., 2021).

Instrument	VCD precision [molec. cm^{-2}]
TROPOMI	6 x 10^{14} – 1 x 10^{15}
OMI	7 x 10^{14} – 1.2 x 10^{15}
GOME-2A	5 x 10^{14} – 7 x 10^{14}
GOME-2B	7 x 10^{14} – 1 x 10^{15}

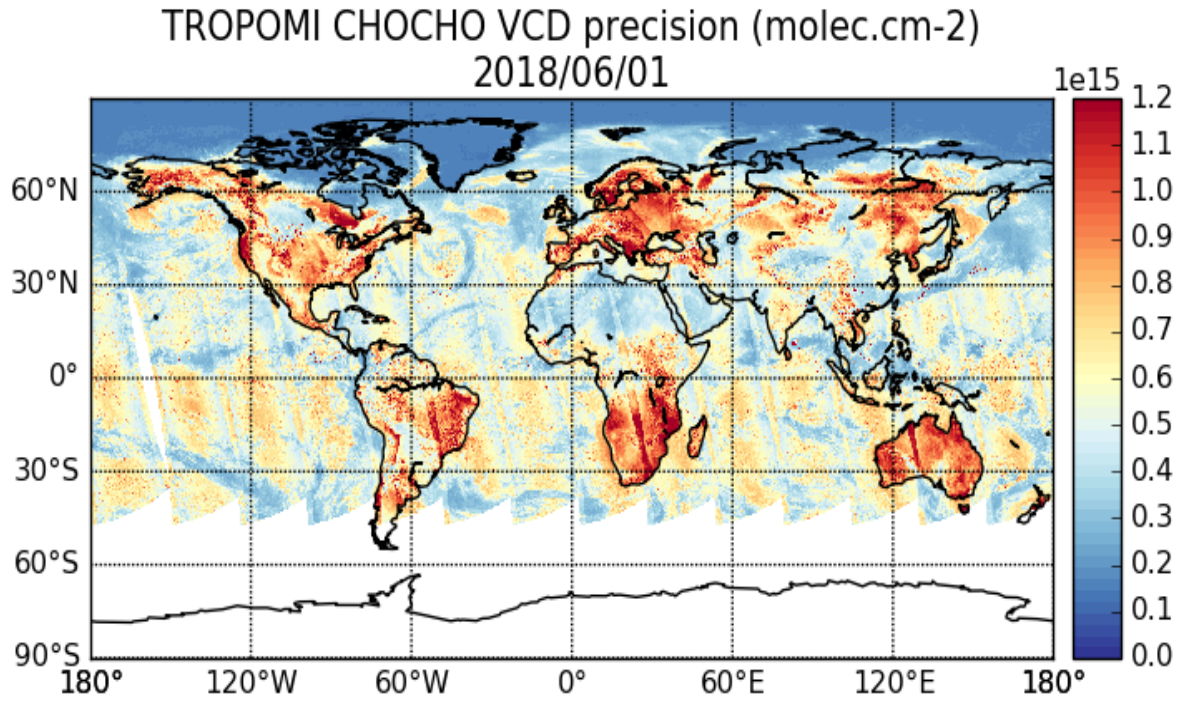

Figure 3.4.1: TROPOMI glyoxal tropospheric column random errors for 1 day, keeping all observations to illustrate the impact of scene brightness.

The total systematic error (trueness) is computed as

$$\sigma^2_{Nv,syst} = \sigma^2_{bck} + \frac{\sigma^2_{Ns,syst}}{M^2} + \frac{\sigma^2_{M,syst} \times N_v^2}{M^2} \quad (3.4\text{-}7)$$

Similarly, the total systematic error without the smoothing error component is calculated as

$$\sigma^2_{Nv,kernel,syst} = \sigma^2_{bck} + \frac{\sigma^2_{Ns,syst}}{M^2} + \frac{\sigma^2_{M,kernel,syst} \times N_v^2}{M^2} \quad (3.4\text{-}8)$$

Note that the conversion of the AMF error into an absolute vertical column error (3rd terms of equations (3.4-7) and (3.4-8) requires this error to be multiplied by the corresponding vertical column. Because of the high level of noise in the product, using the retrieved column for this would lead to a strong overestimation of the systematic error. To circumvent this, we use instead pre-computed climatological glyoxal noise-free VCDs. Figure 3.4.2: shows the mean estimates of the TROPOMI glyoxal VCD trueness for the month of June 2018, which are generally in the range 1-3x10^{14} molec/cm² (20-60% for emission regimes). Note that pixels strongly contaminated by clouds (cloud fraction > 20%) or covered by snow/ice have been discarded. Systematic errors are expected to be larger for those pixels as spectral interferences are larger and the information content becomes limited (cloud shielding effect).

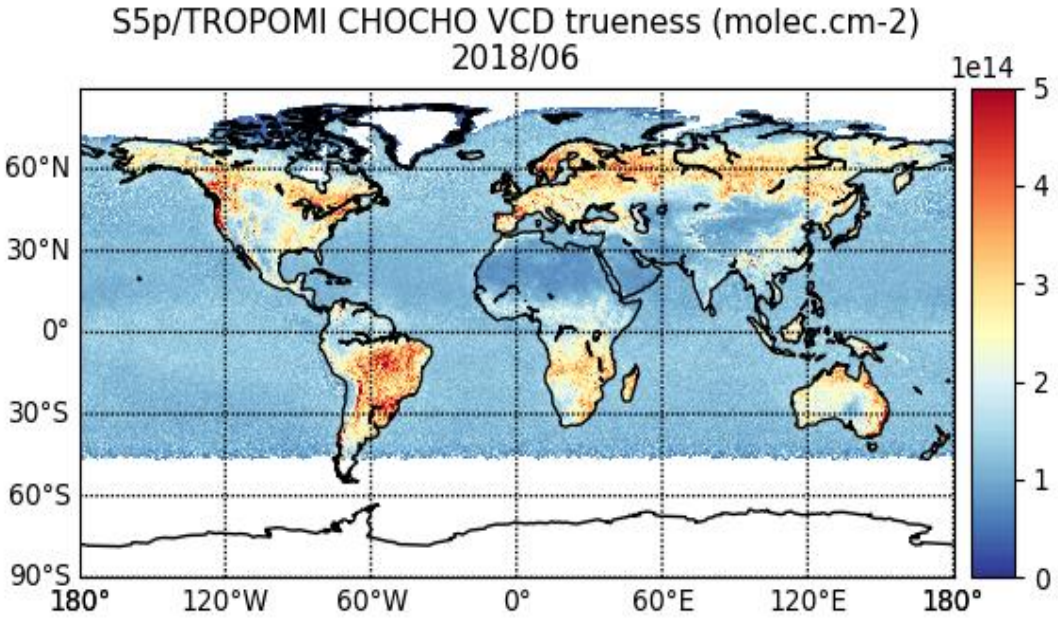

Figure 3.4.2: Mean TROPOMI glyoxal VCD trueness for June 2018.

Table 3.4.2 Glyoxal tropospheric VCD trueness.

Error source	Order of magnitude [molec. cm^{-2}]
Slant column retrieval systematic uncertainty	5 x 10^{13} – 1 x 10^{14}
Air mass factor uncertainty	1 x 10^{13} – 1 x 10^{14}
Background correction uncertainty	5 x 10^{13} – 1 x 10^{14}
Total systematic uncertainty	1 x 10^{14} – 3 x 10^{14}

3.5. Carbon monoxide (L2-CO)

3.5.1. CO uncertainties characterisation

IASI CO L2 data have been retrieved using the Fast Optimal/Operational Retrieval on Layers for IASI (FORLI), a dedicated radiative transfer and retrieval software for IASI. It relies on a scheme based on the Optimal Estimation theory (Rodgers, 2000).

General formulation is given in FORLI Algorithm Theoretical Basis Document (ATBD, Astoreca et al., 2014) and in Hurtmans et al. (2012). In this section, we detail the equations related to the errors or uncertainties.

The Rodergs formalism is the following. By linearizing the inverse model and neglecting the systematic error in the direct and inverse models, the total error on the inverted profile decomposes into three terms:

$$\begin{aligned} \hat{x} - x = (A - I)(x - x_a) \quad & \text{...smoothing error} \\ + G_y K_b\left(b - \hat{b}\right) \quad & \text{...error on the model parameters} \\ + G_y \varepsilon \quad & \text{...error due to radiometric noise} \end{aligned} \tag{3.5-1}$$

With x the unknown state vector,
$\hat{x}$ the retrieval,
A is the sensitivity of the retrieval to the true state ($\frac{\partial \hat{x}}{\partial x}$) (Averaging Kernel matrix)
x_a the a priori profile
G_y the sensitivity of the retrieval to the measurement (Gain matrix)
K_b the sensitivity of the forward model to the forward model parameters
b the model parameters
$\hat{b}$ the estimate of the model parameters

The three components represent respectively :

- the smoothing error: The real state being unknown, the smoothing error can only be estimated if we consider the statistics of this error, described by an average $\bar{x}$ and a covariance of an appropriate ensemble of states, which can be described by the a priori information x_a and S_a. If an ensemble has been chosen for which $\bar{x} = x_a$, the covariance of the smoothing error is:

$$S_s = (A - I)S_a(A - I)^T \tag{3.5-2}$$

- the error on the model parameters, that is to say the inversion error due to the fixed parameters of the direct model. The real state of the parameters b also being unknown, the contribution of this error can only be estimated by considering the covariance matrix associated with the uncertainty on the model parameters S_b, around $\hat{b}$, the best estimate of the parameters. The covariance of this contribution is:

$$S_f = G_y K_b S_b K_b^T G_y^T \quad (3.5\text{-}3)$$

- The error due to radiometric noise, which covariance is:

$$S_m = G_y S_\varepsilon G_y^T \quad (3.5\text{-}4)$$

with S_ε the covariance matrix of the radiometric noise.

In FORLI, the error introduced by uncertainties on the model parameters (e.g. surface emissivity, temperature profile) is not considered.

In conclusion, the covariance matrix representing the total statistical error after the retrieval (also given in Equation 28 of Hurtmans et al.,2012), is the sum of the smoothing error and the radiometric noise error (the smoothing error being dominant).

From the covariance of the smoothing error given in Eq. 3.5-2, substituting A with $G_y K = (K^T S_\varepsilon^{-1} K + S_a^{-1})^{-1} K^T S_\varepsilon^{-1} K$, we obtain:

$$S_s = (K^T S_\varepsilon^{-1} K + S_a^{-1})^{-1} S_a^{-1} (K^T S_\varepsilon^{-1} K + S_a^{-1})^{-1} \quad (3.5\text{-}5)$$

From the covariance of the retrieval noise given in Eq. 3.5-4, we substitute G_y with $(K^T S_\varepsilon^{-1} K + S_a^{-1})^{-1} K^T S_\varepsilon^{-1}$ and we obtain:

$$S_m = (K^T S_\varepsilon^{-1} K + S_a^{-1})^{-1} K^T S_\varepsilon^{-1} K (K^T S_\varepsilon^{-1} K + S_a^{-1})^{-1} \quad (3.5\text{-}6)$$

Finally, the sum of Eq. 3.5-5 and 3.5-6 gives the total error of the two sources:

$$\hat{S} = (K^T S_\varepsilon^{-1} K + S_a^{-1})^{-1} \quad (3.5\text{-}7)$$

In Rodgers formalism, the terminology “error” is used. When retrieving carbon monoxide concentrations from IASI measurements using FORLI, the user gets a “Total Error” with the CO total column, for every pixel.

In section 3.5.2, we performed an analysis of the IASI CO “total error” or uncertainty. First on global scale and then on local scale.

In this document, we performed an analysis of the IASI CO “total error” or uncertainty. First on global scale and then on local scale.

3.5.2. CO uncertainties on global scale

To apprehend CO uncertainties spatial distribution, we first present monthly total uncertainty global distributions, for four months of 2020 in Figure 3.5.1, for daytime and night time measurements. Uncertainties at high latitudes are larger than at mid-latitudes and at the

Tropics, espacially in Boreal winter, when CO concentrations are the largest. Uncertainties are slighly larger during nighttime compared to daytime. When looking at land/sea differences, uncertainties appear to be larger over sea during the day, and larger over land during the night. For daytime measurements, uncertainties are ranging from 0.2 to 5.6 10^{17} molecules/cm^2. For nighttime, uncertainties are ranging from 0.53 to 5.3 10^{17} molecules/cm^2. IASI carbon monoxide total columns are retrieved with an uncertainty generally about 10–15% at mid and tropical latitudes, and 30-40% in the polar regions.

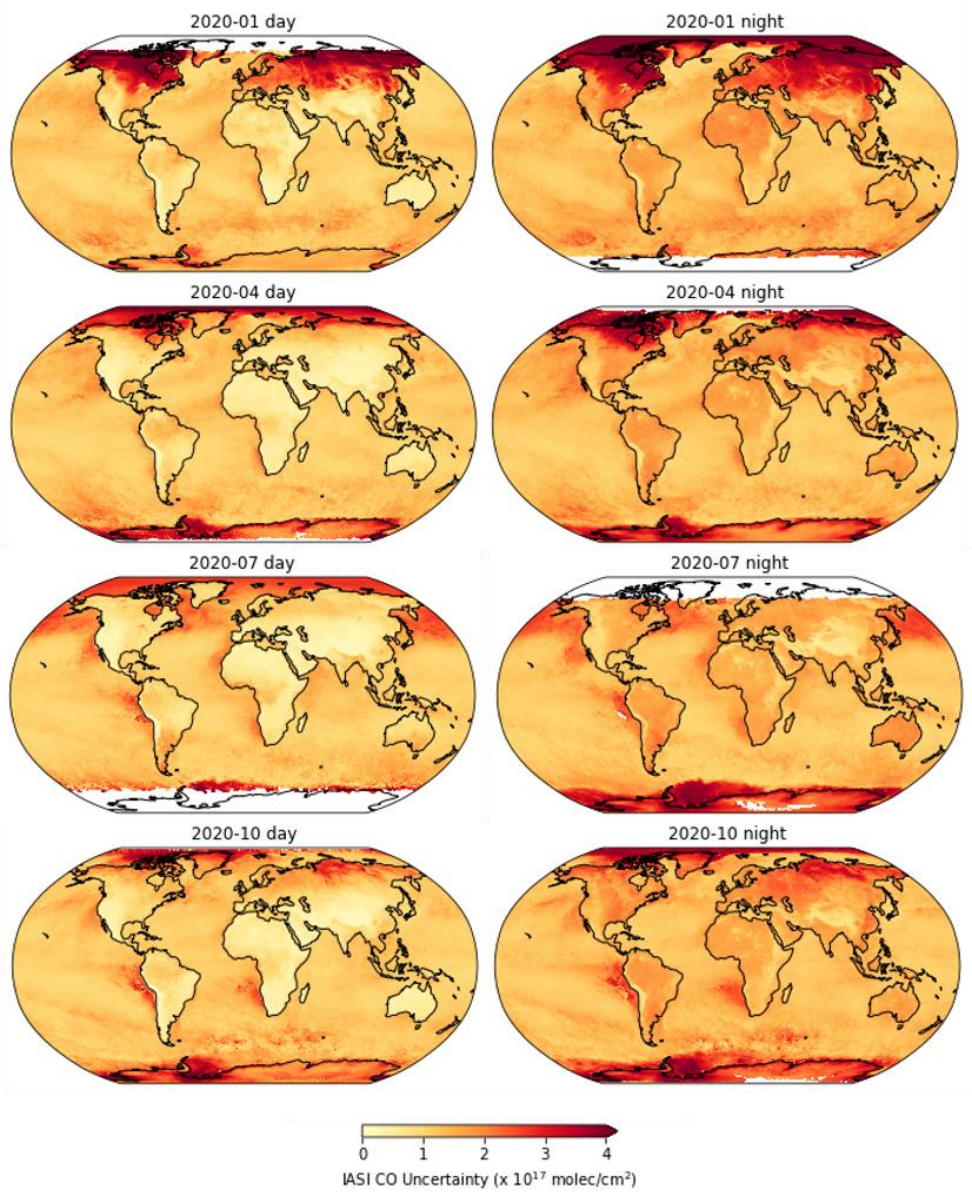

Figure 3.5.1 Monthly CO uncertainty distributions from January, April, July and October 2020, for day time measurements on the left and night time measurements on the right.

For statistics, we focused on different latitude bands and present CO uncertainty time series for Metop-A and B, from January 2008 til December 2021 (see Fig. 3.5.2). On global scale, mean uncertainty for daytime measurements is 1.4 10^{17} molecules/cm^2 with a standard

deviation of 0.1 10^{17} molecules/cm^2 for both Metop-A and Metop-B. For nighttime, the mean uncertainty is larger: 1.7 10^{17} molecules/cm^2 [std: 0.1 10^{17} molecules/cm^2]. For the 20°N-60°N latitude band, mean uncertainty is 1.1 10^{17} molecules/cm^2 [0.1 10^{17}] for daytime, and 1.6 10^{17} molecules/cm^2 [0.1 10^{17}] for nighttime. For the tropical band [20°S-20°N] latitude, mean uncertainty is the smallest compared to the other latitude bands: 1.0 10^{17} molecules/cm^2 [0.02 10^{17}] for daytime, and 1.2 10^{17} molecules/cm^2 [0.02 10^{17}] for nighttime. Finally, for the [60°S-20°S] band, mean uncertainty is 1.3 10^{17} molecules/cm^2 [0.03 10^{17}] for daytime, and 1.4 10^{17} molecules/cm^2 [0.05 10^{17}] for nighttime.

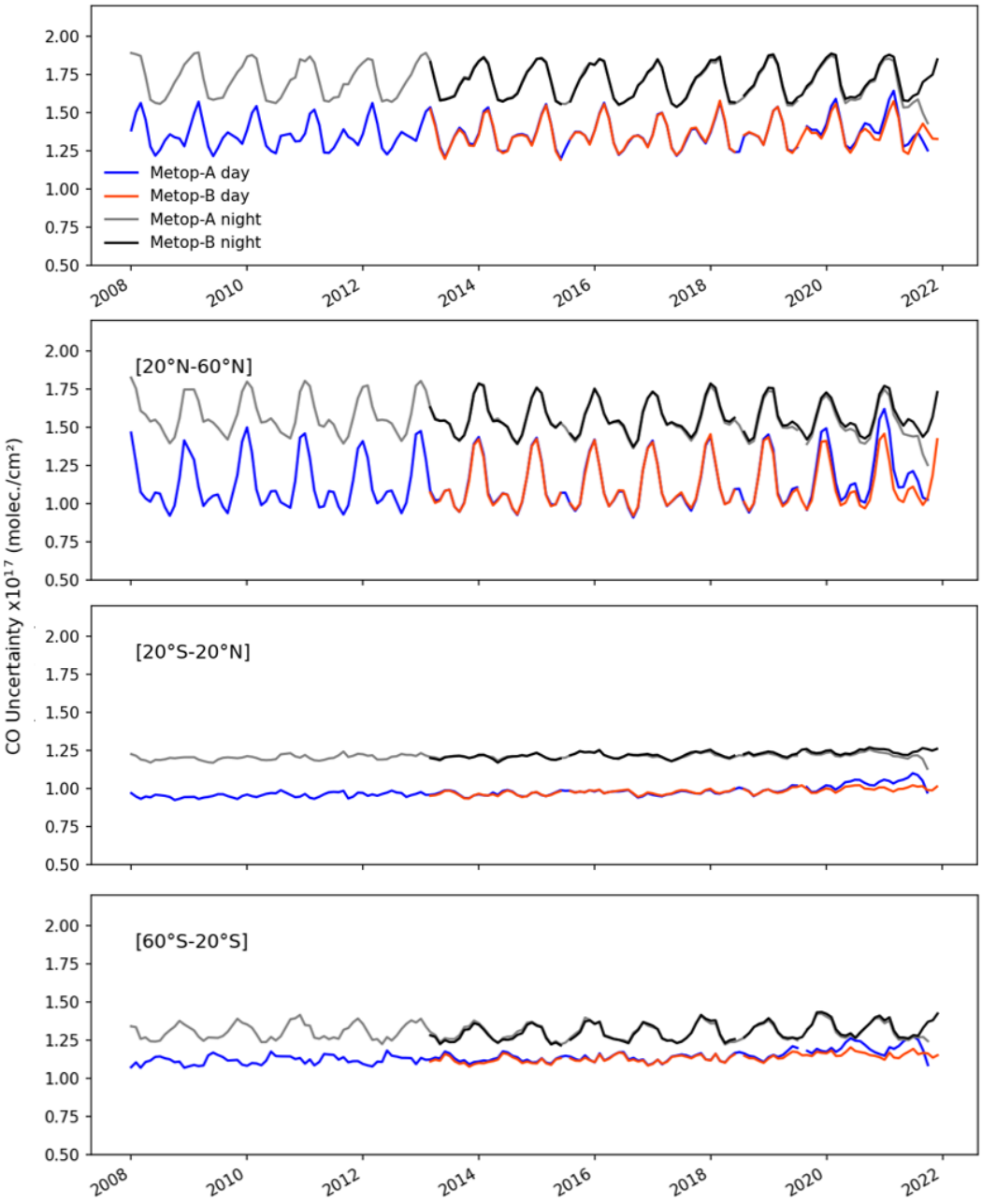

Figure 3.5.2: CO uncertainty time series for the globe (top) and for different latitudes bands: [20°N-60°N], [20°S-20°N] and [60°S-20°S]. For day time and night time measurements.

3.5.3. CO uncertainties on local scale

In order to get uncertainty estimates at local scale, we focused on fifteen locations on the globe, corresponding to TCCON stations (Fig. 3.5.3). Uncertainty time series are presented in Figure 3.5.4. CO uncertainties are following the CO total column concentrations seasonal cycles. Mean uncertainty for each station is given in Table 3.5.1. Over the fifteen stations, mean uncertainties are ranging from 0.63 10^{17} molecules/cm^2 [std 0.27 10^{17}] for Pasadena in the USA (3.2%) to 1.58 10^{17} molecules/cm^2 [std 0.78 10^{17}] (8.4%) in Sodankyla in Finland.

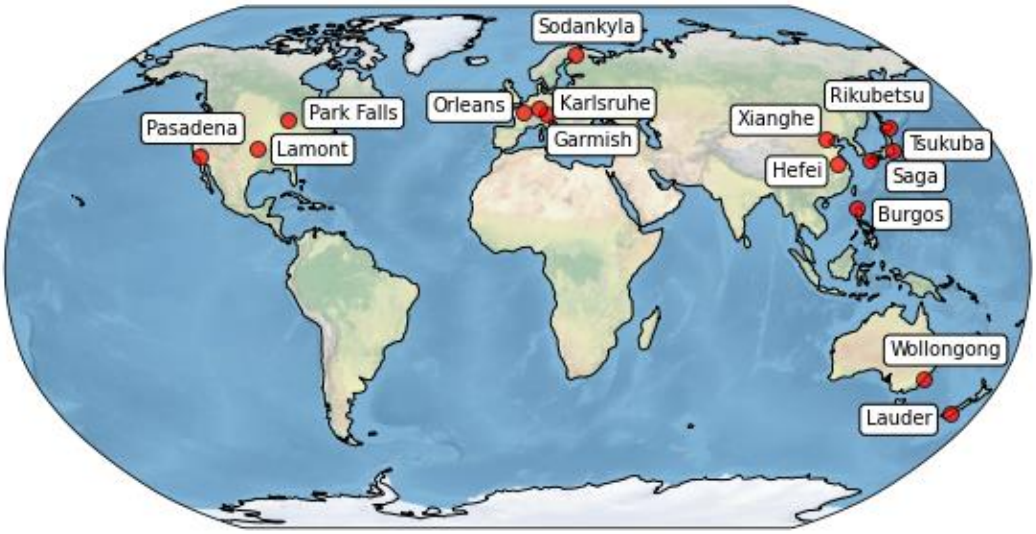

Figure 3.5.3: Location of the fifteen TCCON stations.

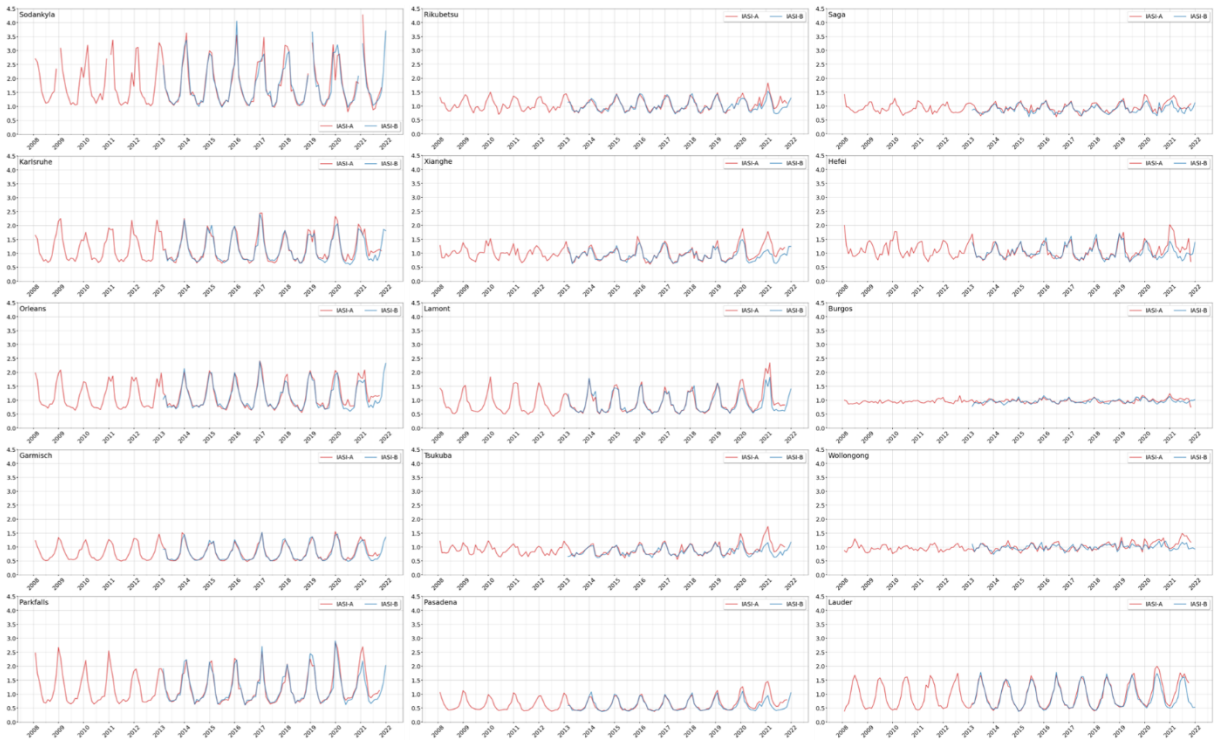

Figure 3.5.4: IASI CO uncertainty (x10^{17} molecules/cm^2) time series at the fifteen TCCON stations presented in Fig. 3.5.3, for Metop-A in red and Metop-B in blue.

Table 3.5.1: Mean uncertainties and standard deviation at the different TCCON stations.

Stations	Mean uncertainty ($x10^{17}$ molec./cm2)	Standard deviation ($x10^{17}$ molec./cm^2)	Mean uncertainty (%)	Standard deviation (percentage point)
Burgos	0.96	0.16	4.5	1.0
Garmisch	0.80	0.32	4.9	2.2
Hefei	1.10	0.36	3.8	1.7
Karlsruhe	1.12	0.56	5.5	3.2
Lamont	0.91	0.49	4.6	2.7
Lauder	0.97	0.50	8.9	4.5
Orleans	1.13	0.56	5.7	3.2
ParkFalls	1.13	0.62	6.2	4.2
Pasadena	0.63	0.27	3.2	1.4
Rikubetsu	1.08	0.30	5.3	2.0
Saga	0.94	0.25	3.9	1.2
Sodankyla	1.58	0.78	8.4	4.8
Tsukuba	0.91	0.29	3.8	1.5
Wollongong	1.01	0.27	7.8	2.1
Xianghe	1.01	0.41	3.7	2.4

3.6. Ammonia (L2-NH3)

The uncertainty assessment of NH_3 has been recently completely reviewed and overhauled (Clarisse et al., 2023). Most of the text below is taken verbatim from this reference.

3.6.1. Uncertainty propagation

In previous ANNI versions, an estimated uncertainty $\sigma_{\hat{X}}$ was calculated for each individual measurement $\hat{X}$ via (Ku, 1966)

$$\sigma_{\hat{X}}^2 = \sum_i \left(\frac{\partial \hat{X}}{\partial p_i}\right)^2 \sigma_{p_i}^2 \quad (3.6\text{-}1)$$

with σ_{p_i} the uncertainties of the different input parameters p_i. This formula assumes uncorrelated uncertainties, but as this cannot always be justified, in ANNI v4, we switch to the more general (Tellinghuisen, 2001)

$$\sigma_{\hat{X}}^2 = \vec{\boldsymbol{J}}^{\mathrm{T}} \boldsymbol{S_p} \vec{\boldsymbol{J}}, \quad (3.6\text{-}2)$$

With $\boldsymbol{S_p}$ the error covariance matrix of the input parameters (with covariances $S_{p,ij} = \sigma_{p_i p_j}$) and $\vec{\boldsymbol{J}}$ the Jacobian of the retrieval, with components $\frac{\partial \hat{X}}{\partial p_i}$.

In the ANNI retrieval framework, the input parameters include the skin temperature, the surface pressure, the HRI, the surface emissivity, the zenith angle, the width, and the peak of the Gaussian vertical NH_3 profile, the temperature profile (15 levels) and the water vapour profile (7 levels). After some preliminary analysis, it was concluded that only the correlations between the uncertainties in the temperature profile cannot be neglected. We therefore employ a block diagonal covariance matrix, block diagonal for the elements pertaining to the temperature profile, and diagonal for all other input parameters. As for uncertainty on the vertical profile, this source of uncertainty is removed when applying averaging kernels. For this reason, uncertainties are reported with and without the vertical profile uncertainty, to be used according to whether AVKs are applied.

3.6.2. Uncertainty on the input parameters

As most input parameters come without an uncertainty budget, let alone covariances, we made best-effort estimates of the co(variance) based on the limited information that is available. For now, the same (co)variances were used for the near-real time as for the reanalysed NH_3 product. It is also important to note that the systematic uncertainties of the input parameters vary according to the time and space scales that are considered (Boersma et al., 2004; Merchant et al., 2017; Sayer et al., 2020). Temperature profiles, for example, may be more biased monthly than annually. Here, we estimate systematic uncertainties with a typical L3 gridded data product in mind, i.e., for spatial scales of the order of one degree latitude/longitude or less, and for time periods of the order of one month or less.

The (co)variances, summarized in Table 3.6.1, were determined as follows:

- **HRI.** By definition, the random uncertainty on the HRI equals one. We estimate a systematic uncertainty of 0.1 due to potential and residual interferences (e.g., surface emissivity, VOCs). To account for potential biases in the spectroscopy and generalized error covariance matrix, we add to this an additional 10% on the calculated HRI value.
- **Skin temperature.** Random and systematic uncertainties were set to 1.5 and 0.5 K respectively. These values are in line with the difference between the IASI L2 skin temperature product and the dedicated neural network used for the reanalysis product of ANNI.
- **Emissivity.** For emissivity, which originates from the monthly climatology of (Zhou et al., 2013), an uncertainty of 0.01 and 0.005 was assumed for respectively the random and systematic components.
- **Temperature profile.** Variances were set based on validation results of the IASI level 2 (Eumetsat, 2021): systematic uncertainties of 1 K for the surface level and 0.5 K for the other levels; random uncertainties of 2 K for the surface level and 1 K for the other levels for land observations and 1 K for the surface level and 0.5 K for the other levels for ocean observations. Covariance matrices were then built by appropriate scaling of correlation matrices. These were built, based on a statistical analysis of the differences between collocated ERA5 and IASI L2 profiles. Correlation coefficients were set to 0.5 between neighbouring levels, and 0.25 between levels that are two levels apart. Above 10 km, no strong correlations were observed, and the covariance was therefore assumed to be diagonal for these levels.
- **Water vapour profiles.** Relying again on the IASI level 2 validation report (Eumetsat, 2021), random uncertainties were set to 10% below 3 km and 20% above. Systematic uncertainties were set to half these numbers.
- **Surface pressure.** A random and systematic uncertainty of 500 and 250 Pa was used.
- **NH_3 vertical profiles.** The uncertainties related to NH_3 profile are characterized by uncertainties on the width and the peak of the Gaussian shaped vertical profile. Random and systematic uncertainties of 200 and 100 m were used for both parameters. Given the short lifetime of NH_3 in the atmosphere, these are likely of the right order of magnitude. To obtain better estimates in the future, a thorough analysis using in-situ measurements or modelled profiles would be desirable.

Table 3.6.5. Estimated random and systematic uncertainties of the input parameters.

Component	Random σ_r	Systematic σ_s
HRI	1	0.1 + 10%
Surface temperature (K)	1.5	0.5
Emissivity	0.01	0.005
Temperature profile, land (K)	1 – 2	0.5 – 1
Temperature profile, sea (K)	0.5 – 1	0.5 – 1
Surface pressure (Pa)	500 Pa	250 Pa
Water vapour profile	10 – 20%	5 – 10%
NH_3 profile peak altitude (m)	200	100
NH_3 profile width (m)	200	100

3.6.3. Uncertainty characterization of L2-NH_3

It is useful, remembering the general form $\hat{X}^a = \mathrm{HRI}/\mathrm{SF}^a$ of the retrieval, to rewrite the propagation of uncertainty in terms of the uncertainty of the nominator and denominator (see also Boersma et al., 2004 and van Geffen et al., 2022). Neglecting the small dependence of the SF on the HRI, we obtain

$$\sigma_{\hat{X}}^2 = \left(\frac{\partial \hat{X}}{\partial \mathrm{HRI}}\right)^2 \sigma_{\mathrm{HRI}}^2 + \left(\frac{\partial \hat{X}}{\partial \mathrm{SF}}\right)^2 \sigma_{\mathrm{SF}}^2 \tag{3.6-3}$$

or

$$\sigma_{\hat{X}}^2 = \frac{\sigma_{\mathrm{HRI}}^2}{\mathrm{SF}^2} + \frac{\sigma_{\mathrm{SF}}^2}{\mathrm{SF}^2} X^2 \tag{3.6-4}$$

Taking into account both random and systematic uncertainties, we see from Table 1 that the uncertainty on the HRI has an absolute (constant) and a relative (proportional to the value of the HRI) component, so that

$$\sigma_{\hat{X}}^2 = \frac{\sigma_{\mathrm{abs,HRI}}^2}{\mathrm{SF}^2} + \frac{\sigma_{\mathrm{rel,HRI}}^2}{\mathrm{SF}^2} + \frac{\sigma_{\mathrm{SF}}^2}{\mathrm{SF}^2} X^2 \tag{3.6-5}$$

or

$$\sigma_{\hat{X}}^2 = \underbrace{\frac{1^2+0.1^2}{\mathrm{SF}^2}}_{\sigma_{\mathrm{abs}}^2} + \underbrace{\left(0.1^2 + \frac{\sigma_{\mathrm{SF}}^2}{\mathrm{SF}^2}\right) X^2}_{\sigma_{\mathrm{rel}}^2} \tag{3.6-6}$$

3.6.3.1. Absolute uncertainty contribution

The first term is in the optically thin limit independent of the HRI and thus the column, and solely depends on the scene conditions:

$$\sigma_{\mathrm{abs}} = \frac{\sigma_{\mathrm{abs,HRI}}}{|\mathrm{SF}|} = \frac{\sqrt{1+0.1^2}}{|\mathrm{SF}|} \approx \frac{1}{|\mathrm{SF}|}. \tag{3.6-7}$$

It is this term that is used as part of the post-filter to determine whether there is enough intrinsic sensitivity (thermal contrast) to make a valid measurement, i.e., one whose uncertainty is not completely overwhelmed by the instrumental noise. Currently, the post-filter threshold is set to $\sigma_{\mathrm{abs}} < 1.5 \cdot 10^{16}$ molec.cm^{-2}. Note also that a scene-dependent detection threshold of the measurements (typically taken as HRI>3), is conveniently expressed in terms of the absolute uncertainty as $X_{\mathrm{thres}} = 3\sigma_{\mathrm{abs}}$.

The absolute uncertainty contribution is illustrated on the left panels of Figure 3.6.1 for the IASI morning overpass (land observations between 60° S and 60° N), as a function of thermal contrast (TC). As before, we define TC as the brightness temperature of the surface minus the temperature at half the boundary layer height. The absolute uncertainty starts from around $1 \cdot 10^{15}$ molec.cm^{-2} and increases as expected with decreasing thermal contrast, with a global

median of $4 \cdot 10^{15}$ molec.cm^{-2}. Observing the inverse proportionality with thermal contrast, the following empirical formula can be used to obtain ballpark estimates of the absolute uncertainty or sensitivity of the IASI NH_3 retrieval (for positive thermal contrasts):

$$\sigma_{\mathrm{abs}} = \frac{3.6 \cdot 10^{16}}{\mathrm{TC}} \frac{\mathrm{molec.\ K}}{\mathrm{cm}^2} \tag{3.6-8}$$

The constants were determined from a fit of the data shown in Figure 3.6.1. Expressed in terms of Q20 and Q80 quantiles the estimated absolute retrieval uncertainty of IASI (mid-latitude, land, morning overpass) can also be summarized as

$$\sigma_{\mathrm{abs}} = [2.5 - 6.6] \cdot 10^{15} \mathrm{molec.cm}^{-2}. \tag{3.6-9}$$

3.6.3.2. Relative uncertainty contribution

The term σ_{rel} is proportional to the column and hence expresses a relative uncertainty for fixed atmospheric conditions:

$$\sigma_{\mathrm{rel}} = \sqrt{0.1^2 + \frac{\sigma_{\mathrm{SF}}^2}{\mathrm{SF}^2}} X \approx \frac{\sigma_{\mathrm{SF}}}{|\mathrm{SF}|} X \tag{3.6-10}$$

or

$$\frac{\sigma_{\mathrm{rel}}}{(X-B)} = \frac{\sigma_{\mathrm{SF}}}{|\mathrm{SF}|} \tag{3.6-11}$$

This term is illustrated on the right panels of Figure 3.6.1. Again, we observe an inverse proportionality with thermal contrast, which can be approximated as

$$\sigma_{\mathrm{rel}} = \left(0.07 + \frac{1.6\mathrm{K}}{\mathrm{TC}}\right) \mathrm{NH}_3. \tag{3.6-12}$$

For typical morning land observations, the relative contribution to the uncertainty starts from around 14% (corresponding to a TC of 20 K). Expressed in terms of Q20 and Q80 quantiles, the estimated relative retrieval uncertainty of ANNI (mid-latitude, land, morning overpass) can be summarized as

$$\sigma_{\mathrm{rel}} = [19 - 36]\%\ \mathrm{NH}_3.$$

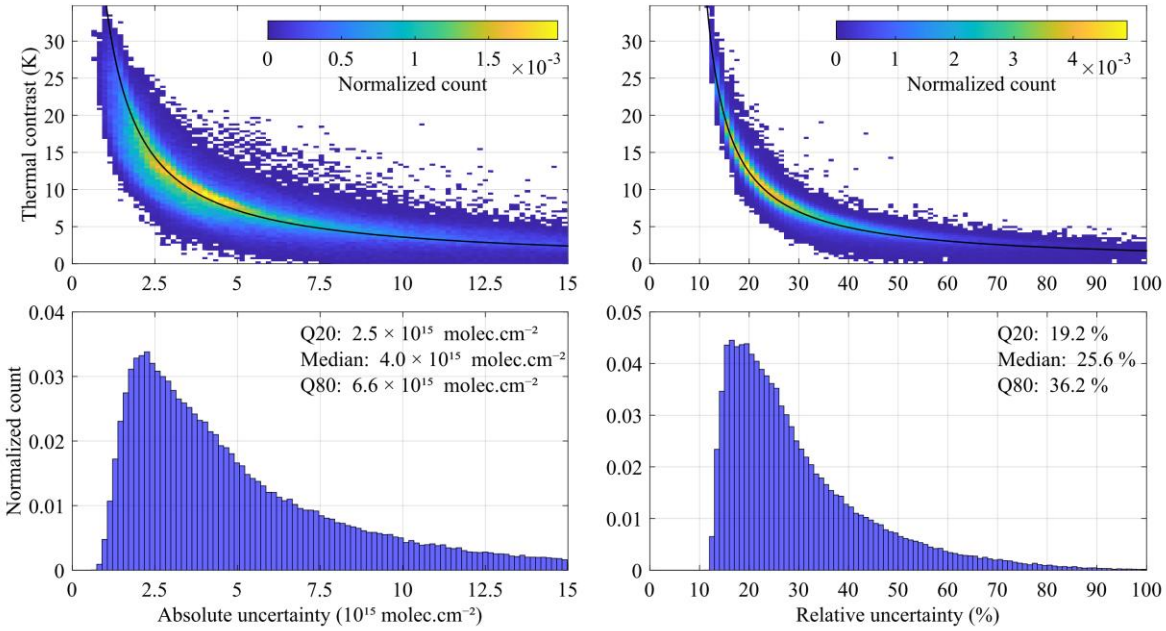

Figure 3.6.3 Illustration of the absolute (left) and relative (right) components of the retrieval uncertainty of NH_3. The top panels illustrate their dependence on thermal contrast, the bottom panels show the normalized count. Data in this plot originates from IASI-B observations on 15 January, April, July and October 2021, morning overpass, land only and between 60° S and 60° N. The approximations from Eq. (3.6.8) and Eq. (3.6.12) are shown in black on the top panels.

4. References

Alvarado, L. M. A., Richter, A., Vrekoussis, M., Wittrock, F., Hilboll, A., Schreier, S. F. and Burrows, J. P.: An improved glyoxal retrieval from OMI measurements, Atmos. Meas. Tech., 7(12), 4133–4150, doi:10.5194/amt-7-4133-2014, 2014.

Anglou, I., Intercomparison of OMI NO2 slant columns and O2-O2 cloud parameters retrieved from Collection 3 and Collection 4 level-1 data, in preparation, 2023.

Astoreca, R., Hurtmans, D., Coheur, P.-F., Fast Optimal Retrieval on Layers for IASI, Algorithm Theoretical Basis Document (ATBD), 2014, available at: https://acsaf.org/docs/atbd/Algorithm_Theoretical_Basis_Document_IASI_CO_Feb_2014.pdf

Beirle, S., Hörmann, C., Jöckel, P., Liu, S., Penning de Vries, M., Pozzer, A., Sihler, H., Valks, P., and Wagner, T.: The STRatospheric Estimation Algorithm from Mainz (STREAM): estimating stratospheric NO_2 from nadir-viewing satellites by weighted convolution, Atmos. Meas. Tech., 9, 2753–2779, https://doi.org/10.5194/amt-9-2753-2016, 2016.

Boersma, K. F., Eskes, H. J., and Brinksma, E. J.: Error analysis for tropospheric NO2 retrieval from space, J. Geophys. Res., 109, D04311, doi: 10.1029/2003JD003962, 2004.

Boersma, K. F., Jacob, D. J., Eskes, H. J., Pinder, R. W., Wang, J., and van der A, R. J.: Intercomparison of SCIAMACHY and OMI tropospheric NO_2 columns: Observing the diurnal evolution of chemistry and emissions from space, *J. Geophys. Res.*, 113, D16S26, doi:10.1029/2007JD008816, 2008.

Boersma, K. F., Eskes, H. J., Dirksen, R. J., van der A, R. J., Veefkind, J. P., Stammes, P., Huijnen, V., Kleipool, Q. L., Sneep, M., Claas, J., Leitão, J., Richter, A., Zhou, Y., and Brunner, D.: An improved tropospheric NO_2 column retrieval algorithm for the Ozone Monitoring Instrument, Atmos. Meas. Tech., 4, 1905-1928, https://doi.org/10.5194/amt-4-1905-2011, 2011.

Boersma, K. F., Vinken, G. C. M., and Eskes, H. J.: Representativeness errors in comparing chemistry transport and chemistry climate models with satellite UV–Vis tropospheric column retrievals, Geosci. Model Dev., 9, 875-898, doi:10.5194/gmd-9-875-2016, 2016.

Boersma, K. F., Eskes, H. J., Richter, A., De Smedt, I., Lorente, A., Beirle, S., van Geffen, J. H. G. M., Zara, M., Peters, E., Van Roozendael, M., Wagner, T., Maasakkers, J. D., van der A, R. J., Nightingale, J., De Rudder, A., Irie, H., Pinardi, G., Lambert, J.-C., and Compernolle, S.: Improving algorithms and uncertainty estimates for satellite NO_2 retrievals: Results from the Quality Assurance for Essential Climate Variables (QA4ECV) project, Atmos. Meas. Tech., 11, 6651-6678, https://doi.org/10.5194/amt-11-6651-2018, 2018.

Castellanos, P., Boersma, K. F., Torres, O., and de Haan, J. F.: OMI tropospheric NO2 air mass factors over South America: effects of biomass burning aerosols, Atmos. Meas. Tech., 8, 3831-3849, doi:10.5194/amt-8-3831-2015, 2015.

Chan Miller, C., Gonzalez Abad, G., Wang, H., Liu, X., Kurosu, T., Jacob, D. J. and Chance, K.: Glyoxal retrieval from the Ozone Monitoring Instrument, Atmos. Meas. Tech., 7(11), 3891–3907, doi:10.5194/amt-7-3891-2014, 2014.

Clarisse, L., Franco, B., Van Damme, M., Di Gioacchino, T., Hadji-Lazaro, J., Whitburn, S., Noppen, L., Hurtmans, D., Clerbaux, C., and Coheur, P.: The IASI NH_3 version 4 product: averaging kernels and improved consistency, Atmos. Meas. Tech. Discuss. [preprint], https://doi.org/10.5194/amt-2023-48, in review, 2023.

Danckaert, T., Fayt, C., van Roozendael, M., De Smedt, I., Letocard, V., Merlaud, A. and Pinardi, G.: QDOAS software user manual. [online] Available from: http://uv-vis.aeronomie.be/software/QDOAS/QDOAS_manual.pdf, 2017.

De Smedt, I., Müller, J.-F., Stavrakou, T., van der A, R., Eskes, H., and Van Roozendael, M.: Twelve years of global observations of formaldehyde in the troposphere using GOME and SCIAMACHY sensors, Atmos. Chem. Phys., 8, 4947–4963, https://doi.org/10.5194/acp-8-4947-2008, 2008.

De Smedt, I., Theys, N., Yu, H., Danckaert, T., Lerot, C., Compernolle, S., Van Roozendael, M., Richter, A., Hilboll, A., Peters, E., Pedergnana, M., Loyola, D., Beirle, S., Wagner, T., Eskes, H., van Geffen, J., Boersma, K. F., and Veefkind, P.: Algorithm theoretical baseline for formaldehyde retrievals from S5P TROPOMI and from the QA4ECV project, Atmos. Meas. Tech., 11, 2395-2426, https://doi.org/10.5194/amt-11-2395-2018, 2018.

De Smedt, I., Pinardi, G., Vigouroux, C., Compernolle, S., Bais, A., Benavent, N., Boersma, F., Chan, K.-L., Donner, S., Eichmann, K.-U., Hedelt, P., Hendrick, F., Irie, H., Kumar, V., Lambert, J.-C., Langerock, B., Lerot, C., Liu, C., Loyola, D., Piters, A., Richter, A., Rivera Cárdenas, C., Romahn, F., Ryan, R. G., Sinha, V., Theys, N., Vlietinck, J., Wagner, T., Wang, T., Yu, H., and Van Roozendael, M.: Comparative assessment of TROPOMI and OMI formaldehyde observations and validation against MAX-DOAS network column measurements, Atmos. Chem. Phys., 21, 12561–12593, https://doi.org/10.5194/acp-21-12561-2021, 2021.

Dirksen, R. J., Boersma, K. F., Eskes, H. J., Ionov, D. V., Bucsela, E. J., Levelt, P. F., and Kelder, H. M.: Evaluation of stratospheric NO_2 retrieved from the Ozone Monitoring Instrument: Intercomparison, diurnal cycle, and trending, J. Geophys. Res., 116, D08305, doi:10.1029/2010JD014943, 2011.

Douros, J., Eskes, H., van Geffen, J., Boersma, K. F., Compernolle, S., Pinardi, G., Blechschmidt, A.-M., Peuch, V.-H., Colette, A., and Veefkind, P.: Comparing Sentinel-5P TROPOMI NO_2 column observations with the CAMS regional air quality ensemble, Geosci. Model Dev., 16, 509–534, https://doi.org/10.5194/gmd-16-509-2023, 2023.

Eskes, H. J., and Boersma, K. F.: Averaging kernels for DOAS total column satellite retrievals, Atmos. Chem. Phys., 3, 1285–1291, 2003.

Eumetsat: Validation, Tech. Rep. EUM/OPS/DOC/19/1091375, https://doi.org/10.15770/EUM_SEC_CLM_0027, 2021.

Huijnen, V., Williams, J., van Weele, M., van Noije, T., Krol, M., Dentener, F., Segers, A., Houweling, S., Peters, W., de Laat, J., Boersma, F., Bergamaschi, P., van Velthoven, P., Le Sager, P., Eskes, H., Alkemade, F., Scheele, R., Nédélec, P., and Pätz, H.-W.: The global chemistry transport model TM5: description and evaluation of the tropospheric chemistry version 3.0, Geosci. Model Dev., 3, 445-473, https://doi.org/10.5194/gmd-3-445-2010, 2010.

Hurtmans, D., Coheur, P., Wespes, C., Clarisse, L., Scharf, O., Clerbaux, C., Hadji-Lazaro, J., George, M. and Turquety, S.: FORLI radiative transfer and retrieval code for IASI. J. Quant. Spectrosc. Radiat. Transfer, 113, 1391-1408, https://doi.org/10.1016/j.jqsrt.2012.02.036, 2012.

Ku, H.: Notes on the use of propagation of error formulas, Journal of Research of the National Bureau of Standards, Section C: Engineering and Instrumentation, 70C, 263, https://doi.org/10.6028/jres.070c.025, 1966.

Lerot, C., Stavrakou, T., De Smedt, I., Müller, J. F., Van Roozendael, M., M̈uller, J. F. and Van Roozendael, M.: Glyoxal vertical columns from GOME-2 backscattered light measurements and comparisons with a global model, Atmos. Chem. Phys., 10(24), 12059–12072, doi:10.5194/acp-10-12059-2010, 2010.

Lerot , C., Stavrakou, T., Van Roozendael, M., Alvarado, L.M.A. and Richter, A.: GLYoxal Retrievals from TROPOMI (GLYRETRO) – ATBD, 2021, available at https://data-portal.s5p-pal.com/product-docs/chocho/CHOCHO_ATBD_S5P+I_BIRA_v3.1.pdf

Lorente, A., Folkert Boersma, K., Yu, H., Dörner, S., Hilboll, A., Richter, A., Liu, M., Lamsal, L. N., Barkley, M., De Smedt, I., Van Roozendael, M., Wang, Y., Wagner, T., Beirle, S., Lin, J. T., Krotkov, N., Stammes, P., Wang, P., Eskes, H. J. and Krol, M.: Structural uncertainty in air mass factor calculation for NO2 and HCHO satellite retrievals, Atmos. Meas. Tech., 10(3), 759–782, doi:10.5194/amt-10-759-2017, 2017.

Liu, M., Lin, J., Boersma, K. F., Pinardi, G., Wang, Y., Chimot, J., Wagner, T., Xie, P., Eskes, H., Van Roozendael, M., Hendrick, F., Wang, P., Wang, T., Yan, Y., Chen, L., and Ni, R.: Improved aerosol correction for OMI tropospheric NO_2 retrieval over East Asia: constraint from CALIOP aerosol vertical profile, Atmos. Meas. Tech., 12, 1-21, https://doi.org/10.5194/amt-12-1-2019, 2019.

Liu, S., Valks, P., Pinardi, G., De Smedt, I., Yu, H., Beirle, S., and Richter, A.: An improved total and tropospheric NO2 column retrieval for GOME-2, Atmos. Meas. Tech., 12, 1029–1057, https://doi.org/10.5194/amt-12-1029-2019, 2019.

Liu, S., Valks, P., Pinardi, G., Xu, J., Argyrouli, A., Lutz, R., Tilstra, L. G., Huijnen, V., Hendrick, F., and Van Roozendael, M.: An improved air mass factor calculation for nitrogen dioxide measurements from the Global Ozone Monitoring Experiment-2 (GOME-2), Atmos. Meas. Tech., 13, 755–787, https://doi.org/10.5194/amt-13-755-2020, 2020.

Merchant, C. J., Paul, F., Popp, T., Ablain, M., Bontemps, S., Defourny, P., Hollmann, R., Lavergne, T., Laeng, A., de Leeuw, G., Mittaz, J., Poulsen, C., Povey, A. C., Reuter, M., Sathyendranath, S., Sandven, S., Sofi eva, V. F., and Wagner, W.: Uncertainty information in climate data records from Earth observation, Earth Syst. Sci. Data, 9, 511–527, https://doi.org/10.5194/essd-9-511-2017, 2017.

Oldeman, A. M.: Effect of including an intensity offset in the DOAS NO2 retrieval of TROPOMI, Internship report, R-1944-SE, Eindhoven University of Technology, Eindhoven, The Netherlands, 2018.

Rodgers, C. D. (2000). *Inverse methods for atmospheric sounding: theory and practice* (Vol. 2). World scientific.

Riess, T. C. V. W., Boersma, K. F., van Vliet, J., Peters, W., Sneep, M., Eskes, H., and van Geffen, J.: Improved monitoring of shipping NO_2 with TROPOMI: decreasing NO_x emissions in European seas during the COVID-19 pandemic, Atmos. Meas. Tech., 15, 1415–1438, https://doi.org/10.5194/amt-15-1415-2022, 2022.

Sayer, A. M., Govaerts, Y., Kolmonen, P., Lipponen, A., Luffarelli, M., Mielonen, T., Patadia, F., Popp, T., Povey, A. C., Stebel, K., and Witek, M. L.: A review and framework for the evaluation of pixel-level uncertainty estimates in satellite aerosol remote sensing, Atmos. Meas. Tech., 13, 373–404, https://doi.org/10.5194/amt-13-373-2020, 2020.

Seo, S., Valks, P., Boersma, K. F., De Smedt, I., Pinardi, G., Liu, S., Richter, A., and Loyola, D.: Development and evaluation of a long-term NO_2 data recored from GOME-2 observations, in preparation, 2023.

Stavrakou, T., Müller, J.-F., De Smedt, I., Van Roozendael, M., van der Werf, G. R., Giglio, L., and Guenther, A.: Evaluating the performance of pyrogenic and biogenic emission inventories against one decade of space-based formaldehyde columns, Atmos. Chem. Phys., 9, 1037–1060, https://doi.org/10.5194/acp-9-1037-2009, 2009.

Tellinghuisen, J.: Statistical Error Propagation, The Journal of Physical Chemistry A, 105, 3917–3921, https://doi.org/10.1021/jp003484u, 2001.

Theys, N., De Smedt, I., Yu, H., Danckaert, T., van Gent, J., Hörmann, C., Wagner, T., Hedelt, P., Bauer, H., Romahn, F., Pedergnana, M., Loyola, D. and Van Roozendael, M.: Sulfur dioxide retrievals from TROPOMI onboard Sentinel-5 Precursor: algorithm theoretical basis, Atmos. Meas. Tech., 10(1), 119–153, doi:10.5194/amt-10-119-2017, 2017.

Theys, N., Fioletov, V., Li, C., De Smedt, I., Lerot, C., McLinden, C., Krotkov, N., Griffin, D., Clarisse, L., Hedelt, P., Loyola, D., Wagner, T., Kumar, V., Innes, A., Ribas, R., Hendrick, F., Vlietinck, J., Brenot, H., and Van Roozendael, M.: A sulfur dioxide Covariance-Based Retrieval Algorithm (COBRA): application to TROPOMI reveals new emission sources, Atmos. Chem. Phys., 21, 16727–16744, https://doi.org/10.5194/acp-21-16727-2021, 2021.

van Geffen, J., Boersma, K. F., Eskes, H., Sneep, M., ter Linden, M., Zara, M., and Veefkind, J. P.: S5P TROPOMI NO_2 slant column retrieval: method, stability, uncertainties and comparisons with OMI, Atmos. Meas. Tech., 13, 1315–1335, https://doi.org/10.5194/amt-13-1315-2020, 2020.

van Geffen, J., Eskes, H., Compernolle, S., Pinardi, G., Verhoelst, T., Lambert, J.-C., Sneep, M., ter Linden, M., Ludewig, A., Boersma, K. F., and Veefkind, J. P.: Sentinel-5P TROPOMI NO_2 retrieval: impact of version v2.2 improvements and comparisons with OMI and ground-based data, Atmos. Meas. Tech., 15, 2037–2060, https://doi.org/10.5194/amt-15-2037-2022, 2022.

Vigouroux, C., Langerock, B., Bauer Aquino, C. A., Blumenstock, T., Cheng, Z., De Mazière, M., De Smedt, I., Grutter, M., Hannigan, J. W., Jones, N., Kivi, R., Loyola, D., Lutsch, E., Mahieu, E., Makarova, M., Metzger, J.-M., Morino, I., Murata, I., Nagahama, T., Notholt, J., Ortega, I., Palm, M., Pinardi, G., Röhling, A., Smale, D., Stremme, W., Strong, K., Sussmann, R., Té,

Y., van Roozendael, M., Wang, P. and Winkler, H.: TROPOMI–Sentinel-5 Precursor formaldehyde validation using an extensive network of ground-based Fourier-transform infrared stations, Atmos. Meas. Tech., 13(7), 3751–3767, doi:10.5194/amt-13-3751-2020, 2020.

Visser, A. J., Boersma, K. F., Ganzeveld, L. N., and Krol, M. C.: European NO_x emissions in WRF-Chem derived from OMI: impacts on summertime surface ozone, Atmos. Chem. Phys., 19, 11821–11841, https://doi.org/10.5194/acp-19-11821-2019, 2019.

Zara, M., Boersma, K. F., De Smedt, I., Richter, A., Peters, E., Van Geffen, J. H. G. M., Beirle, S., Wagner, T., Van Roozendael, M., Marchenko, S., Lamsal, L. N., and Eskes, H. J.: Improved slant column density retrieval of nitrogen dioxide and formaldehyde for OMI and GOME-2A from QA4ECV: intercomparison, uncertainty characterization, and trends, Atmos. Meas. Tech., 11, 4033-4058, https://doi.org/10.5194/amt-11-4033-2018, 2018.

Zhou, D. K., Larar, A. M., and Liu, X.: MetOp-A/IASI Observed Continental Thermal IR Emissivity Variations, IEEE J. Sel. Topics Appl. Earth Observations Remote Sens., 6, 1156–1162, https://doi.org/10.1109/JSTARS.2013.2238892, 2013.